Title

A framework for target discovery in rare cancers

Authors

Bingchen Li[1,‡], Ananthan Sadagopan[1,‡], Jiao Li[1], Yuqianxun Wu[1], Yantong Cui[1], Prathyusha Konda[1], Cary N. Weiss[1,2], Toni K. Choueiri[1,3,4], John G. Doench[5], Srinivas R. Viswanathan[1,3,4,5*]

Affiliations

[1]Department of Medical Oncology, Dana-Farber Cancer Institute; Boston, MA 02215, USA.

[2]Department of Pediatric Oncology, Dana-Farber Cancer Institute; Boston, MA 02215, USA.

[3]Department of Medicine, Harvard Medical School; Boston, MA 02215, USA.

[4]Department of Medicine, Brigham and Women's Hospital; Boston, MA 02215, USA.

[5]Broad Institute of MIT and Harvard; Cambridge, MA 02142, USA.

‡Authors contributed equally.

*To whom correspondence should be addressed: srinivas.viswanathan@dfci.harvard.edu (S.R.V)

Abstract

While large-scale functional genetic screens have uncovered numerous cancer dependencies, rare cancers are poorly represented in such efforts and the landscape of dependencies in many rare cancers remains obscure. We performed genome-scale CRISPR knockout screens in an exemplar rare cancer, *TFE3*-translocation renal cell carcinoma (tRCC), revealing previously unknown tRCC-selective dependencies in pathways related to mitochondrial biogenesis, oxidative metabolism, and kidney lineage specification. To generalize to other rare cancers in which experimental models may not be readily available, we employed machine learning to infer gene dependencies in a tumor or cell line based on its transcriptional profile. By applying dependency prediction to alveolar soft part sarcoma (ASPS), a distinct rare cancer also driven by *TFE3* translocations, we discovered and validated that *MCL1* represents a dependency in ASPS but not tRCC. Finally, we applied our model to predict gene dependencies in tumors from the TCGA (11,373 tumors; 28 lineages) and multiple additional rare cancers (958 tumors across 16 types, including 13 distinct subtypes of kidney cancer), nominating potentially actionable vulnerabilities in several poorly-characterized cancer types. Our results couple unbiased functional genetic screening with a predictive model to establish a landscape of candidate vulnerabilities across cancers, including several rare cancers currently lacking in potential targets.

Main Text

Introduction

A cornerstone of precision oncology is the matching of therapies to specific cancers based on predictive molecular features. Recent advances in the molecular classification of cancer coupled with advances in genome-scale functional genetic screening have enabled the discovery of multiple biomarker-drug pairs that have proven clinically effective in specific cancer subtypes (1–9). Still, limited molecular profiles of rare cancer types and a paucity of robust cellular models for many of these cancers remain barriers to fully realizing the ideal of precision oncology; this is in spite of the fact that many rare cancers have homogeneous genomic landscapes with singular driver alterations that may be directly linked to robust vulnerabilities (10–12).

Kidney cancer is notable in this regard as it comprises dozens of biologically distinct histologies in both adults and children, many of which are quite rare (13). To date, most discovery biology efforts in kidney cancer have focused on clear-cell renal cell carcinoma (ccRCC), which comprises 75% of RCC in adults and is typified by loss of the *VHL* tumor suppressor gene, leading to activation of hypoxia signaling (14). While therapeutic agents targeting this pathway have demonstrated promise in ccRCC (15), other RCC subtypes do not typically harbor *VHL* alterations and are driven by distinct biology (16). It is therefore likely that subtypes of kidney cancer differ in their dependency profiles, though this has not yet been systematically explored.

Translocation renal cell carcinoma (tRCC) is one such subtype of RCC that strikes both adults and children. Molecularly, tRCC is driven by an activating gene fusion involving an MiT/TFE family transcription factor, most commonly *TFE3* (17). Due to a lack of therapies specifically targeted to the biology of tRCC, therapies for ccRCC are frequently used; however, these yield poor response rates (18–23). The discovery of novel molecular targets in tRCC is therefore a pressing unmet need.

Recent studies have revealed few recurrent genomic alterations in tRCC apart from the driver fusion (23–28). Unbiased functional genetic screening can be useful for nominating vulnerabilities in such cases (11,12), but tRCC cell line models have not yet been included in large scale screening efforts (7,29–31), and only a limited number of cell line models of this cancer have been reported (17,32–34). In addition, *TFE3* fusions can drive a spectrum of other rare cancers apart from tRCC, including alveolar soft part sarcoma (ASPS) (35), perivascular epithelioid cell tumor (PEComa) (36), epithelioid haemangioendothelioma (EHE (37), malignant chondroid syringoma (38), and ossifying fibromyxoid tumors (39). It remains unknown whether these tumor types, most of which do not have models amenable to large-scale screening, have distinct dependency

profiles from tRCC despite sharing the same driver fusion. More broadly, many subtypes of kidney cancer apart from ccRCC have limited cellular or *in vivo* models and have been poorly characterized with respect to their molecular features and dependency landscapes.

In this study, we leveraged genome-scale CRISPR screening to discover selective vulnerabilities in tRCC cell line models. To complement this functional data, we applied a machine learning approach to nominate genetic dependencies based on tumor or cell line transcriptome profiles without the need for functional screening. By applying our predictive modeling to a broad range of tumor and cell line RNA-Seq datasets, with a focus on cancers not evaluated or underrepresented in prior functional screening efforts, we present a landscape of candidate vulnerabilities across multiple different *TFE3* fusion cancers, as well as across 13 different molecular subtypes of kidney cancer.

Results

Genome-scale CRISPR knockout screening of tRCC cells

We performed genome-scale pooled CRISPR-Cas9 knockout screening in three tRCC cell lines representing two distinct *TFE3* fusions (FUUR-1: *ASPSCR1-TFE3*; S-TFE: *ASPSCR1-TFE3*; UOK109: *NONO-TFE3*). Each cell line was stably transduced with Cas9 and subsequently transduced with a lentiviral library of 76,441 single-guide RNAs (sgRNAs) targeting 19,114 genes (Broad Brunello library (40)) with 1,000 non-targeting control sgRNAs. Cells were cultured for 28 days, at which point genomic DNA was extracted and sgRNA abundance was compared to the starting pool; sgRNAs depleted from the pool at the conclusion relative to the start of the experiment were inferred to target tRCC-essential genes (**Fig.1A**).

While the Cancer Dependency Map (DepMap) has profiled >1100 cancer cell lines across 28 lineages via genome-scale genetic (RNAi/CRISPR) screening, tRCC cell lines have to date not been included in this effort (30,41). We therefore sought to calibrate our results against published results from the DepMap in order to identify candidate vulnerabilities that are selectively essential in tRCC relative to other cancer types. For each gene assayed in our screens, we calculated a Chronos score, which represents the relative essentiality of a gene accounting for various potential confounders, including sgRNA efficiency, copy number related bias, and heterogenous cutting events (**Methods**) (31); by the Chronos metric, cell-essential genes have a score of approximately -1 while non-essential genes have a score of approximately 0 (31). We compared Chronos scores for each gene in tRCC cells (averaged across the 3 tRCC cell lines screened in our study) to Chronos scores for these same genes in either clear-cell renal cell carcinoma (ccRCC) cell lines (averaged across 14 cell lines) or all cancer lineages (averaged across 1193 cell lines representing 28 lineages, ccRCC excluded) screened in the DepMap (**Fig.1B-C, Supplementary Table S1, Methods**).

Using established lists of essential and non-essential genes(42), we found that essential genes (reported in DepMap) had a mean Chronos score of –0.930 across tRCC cell lines screened in our study, while non-essential genes had a mean Chronos score of -0.026. Importantly, while cell lines in the DepMap effort were screened using the Avana CRISPR knockout sgRNA library (74,687 sgRNAs targeting ~18,560 genes) (40) and the tRCC cell lines in this study utilized the Brunello library, the strong concordance in the scores for both essential and non-essential genes suggests that informative comparisons can be made between our data and those generated via the DepMap effort, despite the use of different genome-scale sgRNA libraries and the screens being conducted over different durations (43).

Among the most selective dependencies in tRCC cells were *TFE3* and *ASPSCR1* (fusion partner of *TFE3* in two of three cell lines screened) (**Fig.1B-C**). *TFE3* fusions typically retain the C-terminal exons of *TFE3* and the N-terminal exons of the fusion partner (23,44). As the Brunello sgRNA library contains 4 sgRNAs per gene, distributed across the gene body, we next sought to determine the log fold-change of individual sgRNAs in each of our CRISPR knockout screens. We found that sgRNAs targeting C-terminal exons of *TFE3* retained within the oncogenic fusion (E, F, G) were strongly depleted in our screens while an sgRNA targeting exon 4

105 (not contained within the oncogenic fusion, H) was not. Similarly, sgRNAs targeting N-terminal exons of the
106 *ASPSCR1* or *NONO* fusion partners were strongly depleted in cell lines containing the *ASPSCR1-TFE3* (s-TFE,
107 FU-UR-1) or *NONO-TFE3* fusions (UOK109), respectively. However, depletion of *NONO* sgRNAs was not
108 observed in s-TFE or FU-UR-1 cells, nor was depletion of *ASPSCR1* sgRNAs observed in UOK109 cells (**Fig.1D**,
109 **Supplementary Fig. S1A)**. We conclude that *TFE3* scores as a strongly selective dependency in tRCC lines due
110 to CRISPR-mediated depletion of the oncogenic driver fusion.

111 To further validate these findings, we performed growth competition assays in tRCC or ccRCC cell
112 lines transduced with Cas9 and either a control sgRNA or an sgRNA targeting *TFE3* (C-terminal region). Strong
113 depletion of *TFE3* knockout cells was observed in all *TFE3*-fusion tRCC cell lines, but not in ccRCC cell lines
114 that express wild type TFE3 (786-O, Caki-1) (**Fig.1E, Supplementary Table S2**). Together, these results
115 indicate that the driver *TFE3* fusion represents the primary selective essentiality in tRCC and that wild type
116 *TFE3* is dispensable in non-fusion cancer cells.

117 **Selectively essential pathways in tRCC**

118 We next sought to discover pathways that might represent selective essentialities in tRCC, beyond the
119 fusion itself. We performed gene ontology enrichment (45) on dependencies selectively essential to tRCC cell
120 lines (defined as ΔChronos ≤ -0.5 between every screened tRCC cell line and either ccRCC cell lines or all
121 lineages in DepMap, **Methods, Supplementary Table S1**). Remarkably, pathways related to oxidative
122 phosphorylation and mitochondrial metabolism were strongly enriched amongst tRCC-selective
123 dependencies (**Fig.2A**, **Supplementary Fig. S1B-C**), and multiple members of biochemical complexes
124 involved in these processes scored as strong selective dependencies in tRCC cells (**Fig.2B-D**). These included:
125 **(1)** genes involved in the transcription and translation of mitochondrially-encoded genes (*POLRMT*:
126 mitochondrial RNA Polymerase that transcribes mitochondrial DNA (mtDNA); *MRPL48*: component of the
127 mitochondrial ribosome ("mitoribosome"); *ERAL1*: involved in mitochondrial rRNA assembly; *NARS2*:
128 mitochondrial asparaginyl tRNA synthetase); **(2)** genes encoding enzymes in the citric acid (TCA) cycle (*SDHA,*
129 *SDHB*); **(3)** genes encoding components of the mitochondrial ATP synthase and electron transport chain
130 (*ATP5F1A, ATP5F1D, ATP5F1E, ATP5ME, ATP5PD, CYCS*); **(4)** genes involved in the assembly or biogenesis of
131 iron-sulfur clusters, which are critical for Complex I, II and III activity within the electron transport chain
132 (46)(*FDX2, HSCB, ISCA1*) (**Fig.2B, E**). Consistent with this screening data, we functionally validated that
133 knockout of several of these genes (*ISCA1, SDHA*, *MRPL48, POLRMT*) selectively impairs the growth of tRCC
134 cells in assays for cell proliferation, cell viability, and clonogenic capacity (**Fig.2F**, **Supplementary Fig. S2A-**
135 **D)**. Altogether, these results strongly validate our recent finding that *TFE3* fusions rewire tRCCs toward
136 oxidative phosphorylation, as opposed to the highly glycolytic metabolism of other kidney cancers (47).

137 Kidney lineage-defining transcription factors (*PAX8*, *HNF1B*) were also strong dependencies in tRCC,
138 as they are in ccRCC **(Fig.1C, Supplementary Fig. S1D)**. PAX8 is a transcription factor in the paired box family
139 that is critical for kidney organogenesis and is broadly expressed in renal epithelial cells as well as in renal
140 parietal cells (48). HNF1B is a homeodomain-containing transcription factor that also plays an important role
141 in nephron development; mutations in this gene represent the most common monogenic cause of
142 developmental renal disease (49). Consistent with these genes being lineage dependencies, knockout of
143 *HNF1B* and *PAX8* was selectively essential to both tRCC and ccRCC cell lines, as previously reported in ccRCC
144 (50), but had no effect on cancer cell lines of other lineages (**Supplementary Fig. S2F-K**). Moreover,
145 dependency of both *PAX8* and *HNF1B* correlated strongly with their expression across the DepMap (*HNF1B*: ρ
146 = -0.42, *P*=1.2e-48; *PAX8*: ρ = -0.26, *P*=2.1e-18) and both genes were highly expressed in tRCC and adjacent
147 kidney-normal tissue, but not in other *TFE3*-driven malignancies (melanotic kidney tumors, PEComa, ASPS)
148 that may be of mesenchymal origin (**Supplementary Fig. S2F-G**). Thus, although tRCCs often display
149 mesenchymal features distinct from most ccRCCs (51), these results functionally suggest that the cancer is
150 of a renal epithelial origin. Three genes involved in mevalonate synthesis (*PMVK, MVK, MVD*) were also strong
151 dependencies in tRCC and had variable levels of dependency across ccRCC cell lines (**Fig.2B-C**,

152 **Supplementary Fig. S2E**); given prior reports of perturbed cholesterol biosynthesis in ccRCC, this may also
153 represent a form of lineage dependency that holds across various types of kidney cancer (52,53).

154 Finally, we uncovered additional strong dependencies that were shared in two of the three screened
155 tRCC cell lines, including cell cycle related genes (*CDK4*), genes involved in hypoxia-inducible factor (HIF)
156 signaling (*EGLN1, VHL*), and genes involved in the antioxidant response (*TXNL4B*, *COA5/6*, *CYC1*)
157 (**Supplementary Fig. S1C**). These represent additional candidate vulnerabilities that could prove
158 therapeutically tractable.

159 **Predicting dependencies in tRCC based on transcriptional profile**

160 The relatively small number of tRCC models available for screening coupled with a diversity in *TFE3*
161 fusion partners and in co-occurring genetic alterations raises the possibility that some strong dependencies
162 may hold only in a subset of tRCC cases. We therefore sought to infer the dependency landscape of a cell line
163 or tumor from its transcriptional profile – a principle that could be broadly applicable since there are many
164 more tumors profiled by RNA sequencing (RNA-Seq) than there are cell line models amenable to large-scale
165 screening, for both tRCC and many other rare cancers.

166 Although it has been suggested that expression profiles may be used to predict vulnerabilities, prior
167 attempts have been applied primarily to cell line models, have had variable performance in tumor samples
168 (53–56), and have not typically been applied with the granularity of cancer subtypes. We sought to establish a
169 machine-learning model to reliably nominate genetic dependencies from cell line models and tumor RNA-Seq
170 data, with a focus on identifying highly predictable dependencies in rare cancer types for which cell line
171 models are not readily available for functional screening. Our pipeline involves merging and normalization of
172 RNA-Seq data from a cell line model or tumor of interest together with reference data (DepMap cell line or
173 TCGA tumor RNA-seq) followed by use of a machine learning model to predict dependencies; we elected to
174 use solely transcriptome profiles for dependency prediction given prior data that expression features have
175 greater predictive power for vulnerabilities than genomic features (54), and to establish the foundation for a
176 streamlined workflow that could be clinically translated (**Fig.3A, Methods**).

177 We first assessed our method on the DepMap dataset; we applied 5-fold cross-validation during the
178 train-test cycle using RNA-Seq expression features from each cell line to calculate a predicted Chronos score
179 for each gene. We elected to limit our predictions to highly predictable gene dependencies (defined as $R \geq 0.4$
180 for predicted vs. experimentally observed Chronos score, averaged across the 5 evaluation folds). We found
181 performance to be maximized with a support vector regression (SVR)-based model (RBF kernel) utilizing the
182 5000 strongest correlated gene expression features for prediction of each dependency. These criteria enabled
183 prediction of dependency scores for 657 genes (hereafter termed predictable dependencies, "PD"). The model
184 was then retrained on the entirety of the DepMap and deployed (**Supplementary Fig. S3A-C, Supplementary**
185 **Table S3, Methods**).

186 We applied our model to calculate predicted dependency scores for PD genes in the three tRCC cell
187 lines for which we had obtained a ground truth via genome-scale CRISPR screening in this study (FU-UR-1, s-
188 TFE, UOK109, **Supplementary Table S4**). We observed a strong correlation between predicted and observed
189 Chronos scores amongst the 657 PD genes in all of these cell lines (FU-UR-1: R=0.71, *P*=4.2e-100; s-TFE:
190 R=0.68, *P*=1.6e-86; UOK109: R=0.62, *P*=3.1e-70) (**Fig.3B**). We also predicted dependency scores in a fourth
191 tRCC cell line (UOK146), on which we had been unable to obtain high-quality genome-scale CRISPR screening
192 data owing to technical limitations (**Fig.3C, Supplementary Table S4**).

193 We nominated selective dependencies in each of these four tRCC cell lines relative to cancer cell lines
194 screened in the DepMap by comparing predicted Chronos scores for PD genes in each cell line to
195 experimentally derived Chronos scores for the same genes in the DepMap. The lineage dependencies *HNF1B*
196 and *PAX8* were prominently identified as selective in all tRCC cell lines, consistent with our screening data in

197 s-TFE, UOK109, and FU-UR-1, above. Mitochondrial superoxide dismutase (*SOD2*), identified in our screen as
198 a dependency in all cell lines (**Supplementary Table S1**, **Fig.2B**), was also a predicted dependency in two of
199 three screened cell lines (s-TFE, FU-UR-1, and narrowly missed the cutoff in the third, UOK109). In addition,
200 two other cell lines were predicted to be selectively dependent on *MDM2* (UOK109, UOK146), the E3 ubiquitin
201 ligase that negatively regulates the p53 tumor suppressor (57). Furthermore, *NFE2L2* and *SLC33A1* (which is
202 synthetically essential with NRF2 activation (58)) were predicted to be a dependency in FU-UR-1 cells (**Fig.3C**).

203 We then applied our dependency prediction to tRCC tumors profiled by RNA-Seq in three independent
204 studies (27,28,59) and again compared predicted Chronos scores to experimentally derived Chronos scores
205 in the DepMap. Reassuringly, dependencies predicted in tRCC cell lines were generally also predicted to be
206 selective dependencies in a subset of tRCC tumors, highlighting the applicability of our pipeline across both
207 cell line models and primary tumor data, and suggesting that existing tRCC models faithfully recapitulate
208 dependencies that would be present in tRCC tumors (**Fig.3D, Supplementary Fig. S3D, Supplementary**
209 **Table S4, Methods**).

210 We sought to validate predicted *MDM2* dependency in a subset of tRCC cell lines and tumors, given
211 that multiple small molecules targeting MDM2 are currently being clinically evaluated for cancer indications
212 (57). Consistent with our predictions, *MDM2* knockout selectively impaired viability and clonogenic capacity
213 in UOK109 and UOK146 cells but not in the other two tRCC cell lines (**Fig.3e, Supplementary Fig. S4A**). This
214 effect was phenocopied by the small molecule MDM2 inhibitor, milademetan, which has shown activity in
215 Phase I clinical trials (60) (**Fig.3F**). To further investigate the reason for divergent responses to milademetan
216 across our four tRCC cell lines, we analyzed whole-exome sequencing data in these cell lines. We observed
217 *TP53* mutations in s-TFE and FU-UR-1 cells (**Supplementary Fig. S4B**), likely explaining the lack of response
218 to milademetan in these two cell lines. Notably, across 88 tRCC tumors from 3 distinct datasets, selective
219 *MDM2* dependency was predicted in most tumors (82/88 [93.2%] tumors with $\Delta\text{Chronos}_{(\text{Predicted-DepMap Mean})} \leq -$
220 0.20, **Supplementary Fig. S3D**). The higher predicted frequency of MDM2-sensitive tRCC tumors relative to
221 cell lines may reflect the selection for *TP53* inactivation upon prolonged cell culture *in vitro*; by contrast,
222 genomic studies have indicated that tRCC tumors are almost always *TP53* wild-type (23,61,62).

223 Finally, we applied our dependency prediction to 20 genes previously reported to be altered in tRCC,
224 even if they were not included in our list of 657 PD genes (23,44). This analysis predicted *KMT2D* to be
225 selectively essential in s-TFE cells relative to other tRCC cell lines (**Supplementary Fig. S4C**), which we
226 validated via arrayed CRISPR/Cas9 knockout **(Supplementary Fig. S4D-E)**. Interestingly, *KMT2D* loss has been
227 associated with metabolic rewiring toward glycolytic metabolism (63). We have recently shown tRCC cells to
228 be dependent on OXPHOS and s-TFE cells have a highly OXPHOS-driven metabolic program (47), which may
229 explain their heightened sensitivity to *KMT2D* knockout.

230 Altogether, these data indicate the ability to predict potentially actionable dependencies from
231 transcriptome profiles of both tRCC cell line models and tumor samples.

232 ***MCL1* dependency in alveolar soft part sarcoma**

233 *TFE3* fusions drive a spectrum of rare cancers apart from tRCC, including alveolar soft part sarcoma
234 (ASPS), some endothelial hemangioendotheliomas (EHE), and some perivascular epithelioid cell tumors
235 (PEComa) (64–66). While these cancers share *TFE3* driver fusions, they may differ in terms of the cell of origin
236 as well as in co-occurring genetic driver alterations. We therefore sought to determine whether the
237 dependency profile of ASPS differs from that of tRCC. We performed RNA-seq on two ASPS cell lines: ASPS-1
238 and ASPS-KY, both of which were too slow-growing to be amenable to genome-scale CRISPR screening, and
239 used our method to predict selective dependencies in ASPS relative to tRCC (**Fig.4A-B, Supplementary Table**
240 **S4**). Similar predictions were performed on published RNA-Seq data from seven ASPS tumors (67). Although
241 the dependency profiles of tRCC and ASPS cell lines were largely concordant (R=0.64), several dependencies
242 were predicted to be selective for ASPS cells versus tRCC, including *MCL1* and *PRKRA*. Conversely, and

consistent with tRCCs being of renal epithelial origin and ASPS being of a mesenchymal origin, the renal lineage dependencies *PAX8* and *HNF1B* were not predicted in ASPS (**Fig.4A-C**, **Supplementary Fig. S3D**).

We also predicted dependencies in PEComa and EHE, two other sarcomas that can be driven by *TFE3* fusions (64,68) and identified vulnerabilities in PD genes that were selective for these malignancies relative to the cell lines experimentally screened in the DepMap, using the procedure described above. Most selective dependencies predicted in these two rare cancers were shared with ASPS (e.g. *FGFR1*, *MCL1*, *PRKAR1A*, *PRKRA*), including the well validated mesenchymal dependency: *GPX4* (69), consistent with all three tumors being sarcomas (**Fig.4C, Supplementary Fig. S5A-C, Supplementary Table S4**).

Targeting of *MCL1* or *PRKRA* by three distinct sgRNAs selectively impaired viability in ASPS cells (ASPS-1 and ASPS-KY) relative to tRCC cells (UOK109, FUUR-1, S-TFE) (**Fig.4D**, **Supplementary Fig. S5D-F**). Similar profiles of differential sensitivity were observed using the clinical-grade MCL1 inhibitor murizatoclax (70) (**Fig.4E**). To gain additional insights into predictors of *MCL1* sensitivity, we identified features predicting *MCL1* dependency in our model across DepMap cell lines; the top predictor was low *BCL2L1* expression (**Fig.4F**). *BCL2L1* encodes the anti-apoptotic factor BCL-xL, which has itself been identified as a dependency in a subset of ccRCC (71). Lower *BCL2L1* expression strongly correlated with greater *MCL1* dependency (ρ=0.50, P=8.2e-71, **Fig.4G**). We further analyzed *BCL2L1* expression in ASPS cell lines/tumors versus tRCC cell lines/tumors and kidney cancer-adjacent normal tissue, when available, and observed substantially lower *BCL2L1* expression in ASPS relative to tRCC and kidney-adjacent normal tissue (**Fig.4H**).

Overall, these analyses highlight the fact that tRCC and ASPS harbor distinct selective vulnerabilities, despite both cancers sharing the same driver fusion; these differences may be linked to a different cell of origin in each tumor.

Predicting dependencies and therapeutic response across cancer types

We next sought to validate our approach across diverse cancer types. We applied our model to predict dependency scores for PD genes for 11,373 tumors representing 33 lineages in The Cancer Genome Atlas (TCGA) (**Supplementary Table S4**). Reassuringly, when clustered (t-distributed Stochastic Neighbor Embedding, t-SNE) on the basis of predicted dependency score, TCGA tumors clustered by lineage together with cell lines experimentally screened in the DepMap (**Supplementary Fig. S6A**). Dependency prediction in the TCGA recovered strong predicted lineage dependencies in the expected patterns, including *SOX10* in melanoma (both cutaneous and uveal) (72,73) and *CTNNB1* in colorectal cancers (74–76) (**Fig.5A)**. Although our model predicts dependency scores based on the top 5000 expression features, relative feature weights may vary widely from gene to gene. In the case of *SOX10* predicted dependency, *SOX10* expression was weighted most heavily, with *CDH19* feature weight being comparable. Notably, *CDH19* is a direct transcriptional target of SOX10 and plays a critical role in neural crest cell development and migration (77). In the case of *CTNNB1*, multiple biologically plausible expression features were linked to β-catenin signaling predicted dependency, including *AXIN2*, *NKD1*, *ASCL2*, and *BMP4* (78–80) (**Fig.5B**). Our modeling also predicted *CDK4* dependency in a subset of cancers across diverse lineages, notably including breast cancer, where CDK4/6 inhibitors are approved but reliable single-gene biomarkers have proven elusive (81). Finally, dependency on glutathione peroxidase 4 (*GPX4*) was predicted to be most pronounced in mesenchymal lineages, consistent with prior studies (69) (**Fig.5A-B**). We conclude that our approach can recover dependencies predicted by outlier expression of one or two genes (e.g. many lineage dependencies) as well as those correlated with more complex expression profiles.

We next sought to infer the dependency profiles of cell line models that have not yet been subjected to unbiased genetic screening. We predicted dependencies in 458 cell lines that were molecularly characterized in the Cancer Cell Line Encyclopedia (CCLE) effort but which have not yet been subjected to genome-scale CRISPR screening in the DepMap (82) **(Supplementary Table S4)**. A subset of these cell lines (restricting to solid tumor lineages with ≥10 cell lines; N=251) were then clustered on the basis of their

289 predicted dependency profile, together with 833 cell lines experimentally screened in the DepMap (using
290 experimentally-derived dependency scores for the latter lines). Reassuringly, cell lines and tumors with
291 predicted dependency profiles clustered primarily with experimentally screened cell lines of the same lineage
292 (**Fig.5C**, **Supplementary Fig. S6A**). However, there were notable and informative exceptions. For example, one
293 cell line of mucinous ovarian origin (JHOM2B) clustered together with screened cell lines of bowel lineage; this
294 was driven by shared dependencies on Wnt pathway members (*CTNNB1*, *TCF7L2*) (74), the Wnt-regulated
295 colon lineage-defining transcription factor *SOX9* (83), and *KRAS* (76) (**Supplementary Fig. S6B**). Notably,
296 treatment of mucinous ovarian cancer with gastrointestinal-type chemotherapy regimens is preferred and
297 associated with better outcomes compared to gynecologic regimens (84). Kidney cancer cell lines also
298 clustered in distinct groups. While a majority of screened and predicted cell lines of kidney origin clustered
299 together (**Fig.5c**), five kidney cancer cell lines, whose dependency scores were predicted, clustered together
300 with screened rhabdoid-like cell lines from distinct lineages (malignant rhabdoid tumors of the kidney,
301 extrarenal rhabdoid tumors, embryonal rhabdomyosarcoma, atypical teratoid/rhabdoid tumors (ATRT), and
302 small cell ovarian cancers (ovarian rhabdoid tumors)) (**Fig.5C**). This co-clustering was driven by shared
303 dependencies on polycomb repressive complex 2 (PRC2) subunits (*EZH2*, *EED*) (85–89) and transcriptional
304 activator *EP300* (90) (**Supplementary Fig. S6C-D**). This implies that a tumor's dependency profile can vary
305 considerably based on histologic subtype and other factors and may not merely reflect the organ from which
306 it is derived.

307 Finally, we explored whether our model could inform response to therapeutic agents with defined
308 molecular targets. While drugs targeting the mammalian target of rapamycin (mTOR) pathway are approved
309 and frequently employed in kidney cancer, accurate biomarkers for patient selection have proven elusive (91).
310 Although *MTOR* was not included in the list of 657 PD genes, it was predicted with reasonable accuracy during
311 testing (R = 0.32, averaged from 5-fold cross-validation). We predicted *MTOR* dependency using tumor RNA-
312 Seq data from patients enrolled in the Checkmate 025 study, a Phase 3 study that compared nivolumab
313 (immune checkpoint inhibitor) with everolimus (mTOR inhibitor) in patients with clear cell renal-cell carcinoma
314 (92). Stratifying by predicted *MTOR* dependency score (median dichotomized), high predicted *MTOR*
315 dependency correlated with better overall (P=0.0078) and progression-free survival (P=0.0381) on the
316 everolimus arm but not the nivolumab arm (OS: P=0.0671, PFS: P=0.9641). Moreover, patients in the
317 everolimus arm with high predicted *MTOR* dependency had similar outcomes to those treated with nivolumab
318 (OS: P=0.3575, PFS: P=0.5949), although nivolumab was superior to everolimus in the overall unselected
319 population (OS: P=0.0069, PFS: P=0.0846) (**Fig.5D**, **Supplementary Fig. S6E)**. Dichotomization by predicted
320 *MTOR* dependency score predicted overall survival on the everolimus arm better than dichotomization using
321 any of the other 657 PD genes (**Supplementary Fig. S6F**). *MTOR* dependency prediction was driven by multiple
322 expression features, with the top predictive feature in DepMap (*DENND2D* expression) also being highly ranked
323 in our model (rank 80/5000) (**Supplementary Fig. S6G**).

324 Together, these results suggest that our approach can be used to both nominate dependencies and
325 inform response to molecularly-targeted therapies across a wide array of tumor types.

326 **A candidate dependency landscape across rare kidney cancers**

327 Having established the tractability of our approach for nominating dependencies across diverse
328 cancer types, we turned our attention to defining the landscape of dependencies across kidney cancers, which
329 comprise a notoriously heterogeneous group of > 40 molecularly distinct subtypes in both adults and children
330 (13). Many of these cancer types have been poorly characterized, are lacking in cell line models amenable to
331 high throughput screening and represent unmet medical needs. We reasoned that dependency prediction
332 could be used to nominate selective dependencies in several of these molecularly-defined entities, in order to
333 better define the spectrum of dependencies across kidney cancer subtypes.

By surveying published studies, we collected RNA-Seq data of 851 tumors across 13 kidney cancer subtypes and used these data to calculate predicted dependency scores for 657 PD genes, as above (**Fig.6A, Supplementary Table S4**). These tumors were then clustered based on dependency profile together with 22 renal cancer cell lines from the DepMap (on which dependency scores were experimentally determined). Group 1 was comprised primarily of ccRCC tumors and most RCC cell lines (which are enriched for clear-cell type (93)), as well as metabolically divergent chRCC (MD-chRCC) tumors. MD-chRCC have been previously described as a distinct, clinically aggressive subset of chRCC with a distinctive hypermethylation pattern and lacking chromosomal losses normally associated with classical chRCC (59). Interestingly, most MD-chRCC tumors demonstrate sarcomatoid differentiation, which may also be seen in a subset of ccRCC tumors (59,94). Group 2 comprised papillary RCC (pRCC type 1 and type 2) as well as a number of diverse entities that have been historically classified as papillary type 2 RCC (95), including CpG island methylator phenotype RCC (CIMP-RCC) and fumarate hydratase (FH)-deficient RCC. Finally, Group 3 consisted of oncocytic tumors, including chRCC and eosinophilic chRCC (**Fig.6B**, **Supplementary Fig. S6H**). Thus, in total, this analysis collapsed 13 distinct subtypes of RCC into three main dependency classes.

We then more carefully interrogated potentially actionable subtype-specific dependencies in kidney cancer. We performed hierarchical clustering of dependency profiles, restricting to 17 genes selective to at least one of the three dependency groups, and including an additional 46 genes with known drug targets. Clustering based on predicted dependency score recapitulated the broad structure observed on t-SNE based clustering above and lent additional insight into specific pairwise comparisons between subtypes (**Fig.6C**). For example, the lineage transcription factors *HNF1B* and *PAX8* were predicted to be very strong dependencies in ccRCC, papillary type 1 and type 2, and most other RCC subtypes with the notable exception of the oncocytic tumors (chRCC, eosinophilic chRCC, oncoytoma, and MD chRCC); this is likely consistent with the former classes of tumors arising from proximal tubule kidney epithelial cells and the latter class arising from mitochondria-rich cells of the distal nephron (96). Notably, *PAX8* and *HNF1B* vary in expression level throughout the nephron, and these gene dependencies are highly correlated to expression level (97,98). Moreover, *HNF1B* is essential for the development of the proximal but not distal tubule(99) (**Fig.6D**, **Supplementary Fig. S2**).

We also observed differential *KEAP1* and *NFE2L2* dependency across RCC subtypes (**Fig.6E**). In particular, FH-deficient RCC and CIMP-RCC were predicted to be strongly dependent on *NFE2L2*, consistent with prior reports of NRF2 pathway activation in these subtypes via methylation of *KEAP1* (CIMP-RCC) or succinylation of *KEAP1* (FH-RCC) (100–102). Although *KEAP1* loss activates NRF2, which is typically oncogenic (103), a subset of RCCs across lineages had predicted dependency scores suggestive of *KEAP1* dependency. This is consistent with recent studies demonstrating that cancers may be sensitive to both oxidative stress (*NFE2L2* dependency) and reductive stress (*KEAP1* dependency), depending on their underlying metabolic features (47,104,105).

Other dependencies appeared to reflect differing rates of genomic alterations across RCC subtypes. For example, *DDX3X* dependency, a paralog dependency known to be unmasked by loss of the Y-chromosome encoded paralog *DDX3Y* (106), was predicted to be among the strongest in pRCC-T1, a tumor type with almost universal somatic loss of the Y chromosome (LOY) (107); accordingly, *DDX3X* dependency was nearly identical between male and female pRCC-T1 samples, but male ccRCC samples (which typically do not show LOY) were far less dependent on *DDX3X,* due to paralog buffering from *DDX3Y* (**Fig.6F**). Most kidney tumors were expected to be dependent on *MDM2*, consistent with the low frequency of *TP53* mutations in this lineage (108); however, *TP53* mutant tumors were predicted to be less *MDM2* dependent than their lineage-matched *TP53* wild-type counterparts (**Supplementary Fig. S6I**).

Dependencies in selenium metabolism (*SEPHS2, SEPSECS, GPX4*), which would be predicted to induce cell death via ferroptosis, were strongest in ccRCC, consistent with prior functional studies in this

380 subtype (109). MD-chRCC also shared this profile, consistent with most MD-chRCCs displaying a
381 mesenchymal signature associated with ferroptosis sensitivity (59,69). Other RCC subtypes also differed in
382 their predicted dependency on various genes involved in apoptotic cell death (*BCL2*, *MCL1*, *BCL2L1*), with FH-
383 deficient RCC and CIMP-RCC predicted to be particularly dependent on *BCL2L1* and oncocytic tumors more
384 dependent on *BCL2*. By contrast to ASPS, as discussed above, few RCCs showed predicted dependency on
385 *MCL1* (**Fig.6G**). Overall, these analyses suggest subtype differences in vulnerabilities to specific modes of cell
386 death.

387 Finally, we sought to nominate dependencies in renal tumors with sarcomatoid and/or rhabdoid
388 differentiation (S/R RCCs) (**Supplementary Table S4**); these aggressive features are thought to represent a
389 dedifferentiation event that can occur in renal tumors of diverse parental histologies (94). Despite being
390 clinically aggressive, immune checkpoint inhibitors appear to be particularly effective in S/R RCC for
391 somewhat unclear reasons and additional treatment strategies for this subset of RCC represent an unmet
392 need (94). Using previously annotated S/R RCCs within the TCGA (94), we identified predicted dependencies
393 that were selective to S/R RCCs. Consistent with de-differentiation of these tumors, we observed lower
394 predicted dependency on kidney lineage transcription factors *HNF1B* and *PAX8* compared to the TCGA pan-
395 kidney cohort. Similar to ASPS and perhaps reflective of a mesenchymal program, we observed greater
396 dependency of S/R RCCs on *MCL1* compared to other kidney tumors. We also observed dependencies in
397 selenium metabolism/ferroptosis vulnerability to be enriched in S/R RCCs including *SEPSECS* and *GPX4* (**Fig.
398 6H, Supplementary Fig. S6J**).

399 Overall, we provide a landscape of dependencies in rare kidney cancers that could be used as a
400 starting point to develop mechanism-inspired therapeutic strategies in these diseases.

401 Discussion

402 In this study, we performed genome-scale CRISPR knockout screening in three cell line models of
403 tRCC, a rare renal tumor not previously included in large scale screening efforts. We identify the *TFE3* fusion
404 as the primary vulnerability in tRCC, consistent with recent genomic studies demonstrating that the fusion
405 represents the dominant, and often sole, driver event in this cancer (23,25–28,44). Given the dispensability *of
406 TFE3* in normal tissues (110) and in all cancer cell lines screened to date in the DepMap, the *TFE3* fusion
407 represents an attractive and highly selective target in tRCC, albeit challenging from the standpoint of
408 druggability.

409 Our study also reveals additional selective vulnerabilities in tRCC, most notably multiple genes
410 involved in mitochondrial metabolism and oxidative phosphorylation, including components of the citric acid
411 (TCA) cycle, mitochondrial transcription and translation, and the electron transport chain. These unbiased
412 screens dovetail remarkably with our recent study demonstrating that TFE3 fusions metabolically rewire
413 tRCCs towards oxidative phosphorylation (OXPHOS) via transcriptional activation of multiple genes involved
414 in oxidative metabolism and mitochondrial biogenesis (47). They are also consistent with the role of wild type
415 TFE proteins as critical regulators of energy metabolism (111–113). Individual genes within these or related
416 pathways may represent more tractable therapeutic targets than the fusion itself and may represent inroads
417 to modulate critical downstream pathways driven by TFE3.

418 However, our tRCC screens also highlight a critical limitation of unbiased functional genomics in rare
419 cancers - namely, the number and availability of suitable models. Over fifteen different *TFE3* fusion partners
420 have been reported (23), but only two distinct fusions were represented in the three cell lines screened in this
421 study. For example, we found the tRCC cell line UOK146, which harbors the relatively common *PRCC-TFE3*
422 fusion (23), to be not technically amenable to genome-scale CRISPR knockout screening. Additionally, while
423 ASPS is also driven by a TFE3-fusion, available ASPS cell lines are slow growing and challenging to culture at
424 the scale required for genome-scale screening. Many other rare adult and pediatric malignancies that would

425 benefit from targeted therapeutics have not been included in unbiased functional screening efforts due to their
426 rarity or due to existing models being unamenable to screening.

427 We attempted to bridge this gap by pursuing the alternative approach of predicting a tumor's
428 dependency landscape via its transcriptional profile. Recent studies have reported approaches to predict a
429 tumor's dependency profile by virtue of its transcriptional and/or genomic features (54,56,114). While each of
430 these models differs somewhat in approach, all are complementary and formal benchmarking would be
431 required to hone the most accurate method for predicting tumor vulnerabilities. Our approach utilizes
432 predictive expression features that can be readily obtained by clinical transcriptome sequencing of tumor
433 tissue and we suggest that this or a similar approach can be broadly useful to guide treatment selection in rare
434 cancers, for which there is often no evidence-based standard of care. This approach may also be developed
435 to therapies that have a clearly defined molecular target (e.g. everolimus) but no robust biomarker in clinical
436 use.

437 We predict and validate dependencies across a host of rare cancer types not well-represented in the
438 TCGA and validate several key examples. Via this approach we identified differential dependencies between
439 tRCC and ASPS despite both cancers sharing the same driver fusion, with ASPS cells being selectively sensitive
440 to MCL1 inhibition. Notably, multiple MCL1 inhibitors have advanced clinically; although cardiac toxicity has
441 proven a challenge to earlier agents, newer MCL1 inhibitors appear not to have this liability (115,116). Our
442 study suggests that CDK4/6 inhibitors, EGLN1 inhibitors (47), and MDM2 inhibitors represent additional
443 classes of agents with clinically advanced molecules that could be tested for activity in tRCC or ASPS.

444 Finally, by applying dependency prediction to a spectrum of kidney cancers, we suggest that kidney
445 cancer subtypes have notably distinct dependency landscapes. Remarkably, although there are several dozen
446 histologic types of kidney cancer, many with multiple expression subtypes (13), we find that kidney cancers
447 collapse into three main groups in dependency space. Intriguingly, S/R RCCs (which can be derived from
448 various RCC subtypes) span multiple dependency clusters and share a small set of unique dependencies.
449 Most discovery biology in kidney cancer has to date has focused on ccRCC: while this has resulted in marked
450 improvements in the treatment of ccRCC over the last decade, these therapies are typically less effective in
451 non-ccRCCs (117), which may be driven by distinct biology. Dependencies related to energy metabolism
452 encapsulate this notion: while deficiency in TCA cycle enzymes such as FH and SDHA/B drives tumorigenesis
453 in glycolytic renal cancers (e.g. FH-RCC and ccRCC), these same genes represent dependencies in high
454 OXPHOS renal cancers such as tRCC (47). We nominate several potentially actionable dependencies,
455 including BCL-xL (*BCL2L1*), *DDX3X*, and *NFE2L2* that may represent novel therapeutic targets in subsets of
456 kidney cancer.

457 Overall, we suggest that our combined approach of functional screening and dependency prediction
458 may catalyze precision oncology in many settings, particularly for rare cancers and in many pediatric cancers,
459 where experimental models may be limited, or where discovery biology efforts are resource-limited by small
460 commercial markets and modest industry investment.

461 ## References

462 1. Konda P, Garinet S, Van Allen EM, Viswanathan SR. Genome-guided discovery of cancer
463 therapeutic targets. Cell Reports. 2023;42:112978.

464 2. Hahn WC, Bader JS, Braun TP, Califano A, Clemons PA, Druker BJ, et al. An expanded
465 universe of cancer targets. Cell. 2021;184:1142–55.

466 3. Garraway LA, Lander ES. Lessons from the Cancer Genome. Cell. 2013;153:17–37.

467 4. MacConaill LE, Garraway LA. Clinical Implications of the Cancer Genome. JCO. Wolters
468 Kluwer; 2010;28:5219–28.

469 5. Basu A, Bodycombe NE, Cheah JH, Price EV, Liu K, Schaefer GI, et al. An interactive resource
470 to identify cancer genetic and lineage dependencies targeted by small molecules. Cell.
471 2013;154:1151–61.

472 6. Parrish PCR, Thomas JD, Gabel AM, Kamlapurkar S, Bradley RK, Berger AH. Discovery of
473 synthetic lethal and tumor suppressor paralog pairs in the human genome. Cell Reports.
474 2021;36:109597.

475 7. Behan FM, Iorio F, Picco G, Gonçalves E, Beaver CM, Migliardi G, et al. Prioritization of
476 cancer therapeutic targets using CRISPR–Cas9 screens. Nature. 2019;568:511–6.

477 8. Pacini C, Duncan E, Gonçalves E, Gilbert J, Bhosle S, Horswell S, et al. A comprehensive
478 clinically informed map of dependencies in cancer cells and framework for target
479 prioritization. Cancer Cell. Elsevier; 2024;42:301-316.e9.

480 9. Viswanathan SR, Nogueira MF, Buss CG, Krill-Burger JM, Wawer MJ, Malolepsza E, et al.
481 Genome-scale analysis identifies paralog lethality as a vulnerability of chromosome 1p loss
482 in cancer. Nat Genet. 2018;50:937–43.

483 10. Jamshidi F, Nielsen TO, Huntsman DG. Cancer genomics: why rare is valuable. J Mol Med.
484 2015;93:369–81.

485 11. Dharia NV, Kugener G, Guenther LM, Malone CF, Durbin AD, Hong AL, et al. A first-
486 generation pediatric cancer dependency map. Nat Genet. Nature Publishing Group;
487 2021;53:529–38.

488 12. Sharifnia T, Wawer MJ, Goodale A, Lee Y, Kazachkova M, Dempster JM, et al. Mapping the
489 landscape of genetic dependencies in chordoma. Nat Commun. 2023;14:1933.

490 13. Moch H, Cubilla AL, Humphrey PA, Reuter VE, Ulbright TM. The 2016 WHO Classification of
491 Tumours of the Urinary System and Male Genital Organs—Part A: Renal, Penile, and
492 Testicular Tumours. European Urology. 2016;70:93–105.

493 14. Schödel J, Grampp S, Maher ER, Moch H, Ratcliffe PJ, Russo P, et al. Hypoxia, Hypoxia-
494 inducible Transcription Factors, and Renal Cancer. European Urology. 2016;69:646–57.

495 15. Shirole NH, Kaelin WG. von-Hippel Lindau and Hypoxia-Inducible Factor at the Center of
496 Renal Cell Carcinoma Biology. Hematol Oncol Clin North Am. 2023;37:809–25.

497 16. John A, Spain L, Hamid AA. Navigating the Current Landscape of Non-Clear Cell Renal Cell
498 Carcinoma: A Review of the Literature. Current Oncology. Multidisciplinary Digital Publishing
499 Institute; 2023;30:923–37.

500 17. Kauffman EC, Ricketts CJ, Rais-Bahrami S, Yang Y, Merino MJ, Bottaro DP, et al. Molecular
501 genetics and cellular features of TFE3 and TFEB fusion kidney cancers. Nat Rev Urol.
502 2014;11:465–75.

503 18. Choueiri TK, Lim ZD, Hirsch MS, Tamboli P, Jonasch E, McDermott DF, et al. Vascular
504 endothelial growth factor-targeted therapy for the treatment of adult metastatic Xp11.2
505 translocation renal cell carcinoma. Cancer. 2010;116:5219–25.

506 19. Malouf GG, Camparo P, Oudard S, Schleiermacher G, Theodore C, Rustine A, et al. Targeted
507 agents in metastatic Xp11 translocation/TFE3 gene fusion renal cell carcinoma (RCC): a
508 report from the Juvenile RCC Network. Ann Oncol. 2010;21:1834–8.

509 20. Boilève A, Carlo MI, Barthélémy P, Oudard S, Borchiellini D, Voss MH, et al. Immune
510 checkpoint inhibitors in MITF family translocation renal cell carcinomas and genetic
511 correlates of exceptional responders. j immunotherapy cancer. 2018;6:159.

512 21. Chanzá NM, Xie W, Bilen MA, Dzimitrowicz H, Burkart J, Geynisman DM, et al. Cabozantinib
513 in advanced non-clear-cell renal cell carcinoma: a multicentre, retrospective, cohort study.
514 Lancet Oncol. 2019;20:581–90.

515 22. Alhalabi O, Thouvenin J, Négrier S, Vano Y-A, Campedel L, Hasanov E, et al. Immune
516 Checkpoint Therapy Combinations in Adult Advanced MiT Family Translocation Renal Cell
517 Carcinomas. The Oncologist. 2023;28:433–9.

518 23. Bakouny Z, Sadagopan A, Ravi P, Metaferia NY, Li J, AbuHammad S, et al. Integrative clinical
519 and molecular characterization of translocation renal cell carcinoma. Cell Rep.
520 2022;38:110190.

521 24. Malouf GG, Monzon FA, Couturier J, Molinié V, Escudier B, Camparo P, et al. Genomic
522 heterogeneity of translocation renal cell carcinoma. Clin Cancer Res. 2013;19:4673–84.

523 25. Malouf GG, Su X, Yao H, Gao J, Xiong L, He Q, et al. Next-generation sequencing of
524 translocation renal cell carcinoma reveals novel RNA splicing partners and frequent
525 mutations of chromatin-remodeling genes. Clin Cancer Res. 2014;20:4129–40.

526 26. Marcon J, DiNatale RG, Sanchez A, Kotecha RR, Gupta S, Kuo F, et al. Comprehensive
527 Genomic Analysis of Translocation Renal Cell Carcinoma Reveals Copy-Number Variations
528 as Drivers of Disease Progression. Clin Cancer Res. 2020;26:3629–40.

529 27. Sun G, Chen J, Liang J, Yin X, Zhang M, Yao J, et al. Integrated exome and RNA sequencing of
530 TFE3-translocation renal cell carcinoma. Nat Commun. Nature Publishing Group;
531 2021;12:5262.

532 28. Qu Y, Wu X, Anwaier A, Feng J, Xu W, Pei X, et al. Proteogenomic characterization of MiT
533 family translocation renal cell carcinoma. Nat Commun. Nature Publishing Group;
534 2022;13:7494.

535 29. Meyers RM, Bryan JG, McFarland JM, Weir BA, Sizemore AE, Xu H, et al. Computational
536 correction of copy number effect improves specificity of CRISPR-Cas9 essentiality screens
537 in cancer cells. Nat Genet. 2017;49:1779–84.

538 30. Tsherniak A, Vazquez F, Montgomery PG, Weir BA, Kryukov G, Cowley GS, et al. Defining a
539 Cancer Dependency Map. Cell. 2017;170:564-576.e16.

31. Dempster JM, Boyle I, Vazquez F, Root DE, Boehm JS, Hahn WC, et al. Chronos: a cell population dynamics model of CRISPR experiments that improves inference of gene fitness effects. Genome Biol. 2021;22:343.

32. Ishiguro M, Iwasaki H, Ohjimi Y, Kaneko Y. Establishment and characterization of a renal cell carcinoma cell line (FU-UR-1) with the reciprocal ASPL-TFE3 fusion transcript. Oncol Rep. 2004;11:1169–75.

33. Hirobe M, Masumori N, Tanaka T, Kitamura H, Tsukamoto T. Establishment of an ASPL-TFE3 renal cell carcinoma cell line (S-TFE). Cancer Biol Ther. 2013;14:502–10.

34. Calandrini C, Schutgens F, Oka R, Margaritis T, Candelli T, Mathijsen L, et al. An organoid biobank for childhood kidney cancers that captures disease and tissue heterogeneity. Nat Commun. 2020;11:1310.

35. Fujiwara T, Kunisada T, Nakata E, Nishida K, Yanai H, Nakamura T, et al. Advances in treatment of alveolar soft part sarcoma: an updated review. Jpn J Clin Oncol. 2023;53:1009–18.

36. Argani P, Gross JM, Baraban E, Rooper LM, Chen S, Lin M-T, et al. TFE3 -Rearranged PEComa/PEComa-like Neoplasms : Report of 25 New Cases Expanding the Clinicopathologic Spectrum and Highlighting its Association With Prior Exposure to Chemotherapy. Am J Surg Pathol. 2024;48:777–89.

37. Neil E, Kouskoff V. Current Model Systems for Investigating Epithelioid Haemangioendothelioma. Cancers (Basel). 2023;15:3005.

38. Panagopoulos I, Gorunova L, Lund-Iversen M, Bassarova A, Heim S. Fusion of the Genes PHF1 and TFE3 in Malignant Chondroid Syringoma. Cancer Genomics Proteomics. 2019;16:345–51.

39. Suurmeijer AJH, Song W, Sung Y-S, Zhang L, Swanson D, Fletcher CDM, et al. Novel recurrent PHF1-TFE3 fusions in ossifying fibromyxoid tumors. Genes Chromosomes Cancer. 2019;58:643–9.

40. Doench JG, Fusi N, Sullender M, Hegde M, Vaimberg EW, Donovan KF, et al. Optimized sgRNA design to maximize activity and minimize off-target effects of CRISPR-Cas9. Nat Biotechnol. 2016;34:184–91.

41. DepMap, Broad (2024). Current DepMap Release data, including CRISPR Screens, PRISM Drug Screens, Copy Number, Mutation, Expression, and Fusions. DepMap 23Q2 Public. Figshare+. Dataset.;

42. Hart T, Chandrashekhar M, Aregger M, Steinhart Z, Brown KR, MacLeod G, et al. High-Resolution CRISPR Screens Reveal Fitness Genes and Genotype-Specific Cancer Liabilities. Cell. 2015;163:1515–26.

575 43. Dempster JM, Pacini C, Pantel S, Behan FM, Green T, Krill-Burger J, et al. Agreement between
576 two large pan-cancer CRISPR-Cas9 gene dependency data sets. Nat Commun.
577 2019;10:5817.

578 44. Achom M, Sadagopan A, Bao C, McBride F, Xu Q, Konda P, et al. A genetic basis for cancer
579 sex differences revealed in Xp11 translocation renal cell carcinoma [Internet]. bioRxiv; 2023
580 [cited 2023 Aug 9]. page 2023.08.04.552029. Available from:
581 https://www.biorxiv.org/content/10.1101/2023.08.04.552029v1

582 45. Kuleshov MV, Jones MR, Rouillard AD, Fernandez NF, Duan Q, Wang Z, et al. Enrichr: a
583 comprehensive gene set enrichment analysis web server 2016 update. Nucleic Acids Res.
584 2016;44:W90-97.

585 46. Read AD, Bentley RE, Archer SL, Dunham-Snary KJ. Mitochondrial iron-sulfur clusters:
586 Structure, function, and an emerging role in vascular biology. Redox Biol. 2021;47:102164.

587 47. Li J, Huang K, McBride F, Sadagopan A, Gallant DS, Thakur M, et al. TFE3 fusions direct an
588 oncogenic transcriptional program that drives OXPHOS and unveils vulnerabilities in
589 translocation renal cell carcinoma [Internet]. bioRxiv; 2024 [cited 2024 Aug 10]. page
590 2024.08.09.607311. Available from:
591 https://www.biorxiv.org/content/10.1101/2024.08.09.607311v1

592 48. Tong G-X, Yu WM, Beaubier NT, Weeden EM, Hamele-Bena D, Mansukhani MM, et al.
593 Expression of PAX8 in normal and neoplastic renal tissues: an immunohistochemical study.
594 Modern Pathology. 2009;22:1218–27.

595 49. Clissold RL, Hamilton AJ, Hattersley AT, Ellard S, Bingham C. HNF1B-associated renal and
596 extra-renal disease—an expanding clinical spectrum. Nat Rev Nephrol. 2015;11:102–12.

597 50. Patel SA, Hirosue S, Rodrigues P, Vojtasova E, Richardson EK, Ge J, et al. The renal lineage
598 factor PAX8 controls oncogenic signalling in kidney cancer. Nature. 2022;606:999–1006.

599 51. Prakasam G, Mishra A, Christie A, Miyata J, Carrillo D, Tcheuyap VT, et al. Comparative
600 genomics incorporating translocation renal cell carcinoma mouse model reveals molecular
601 mechanisms of tumorigenesis. J Clin Invest. 2024;134:e170559.

602 52. Riscal R, Bull CJ, Mesaros C, Finan JM, Carens M, Ho ES, et al. Cholesterol Auxotrophy as a
603 Targetable Vulnerability in Clear Cell Renal Cell Carcinoma. Cancer Discovery.
604 2021;11:3106–25.

605 53. Thompson JM, Alvarez A, Singha MK, Pavesic MW, Nguyen QH, Nelson LJ, et al. Targeting the
606 Mevalonate Pathway Suppresses VHL-Deficient CC-RCC through an HIF-Dependent
607 Mechanism. Molecular Cancer Therapeutics. 2018;17:1781–92.

608 54. Dempster JM, Krill-Burger JM, McFarland JM, Warren A, Boehm JS, Vazquez F, et al. Gene
609 expression has more power for predicting *in vitro* cancer cell vulnerabilities than genomics
610 [Internet]. 2020 [cited 2024 Jun 26]. Available from:
611 http://biorxiv.org/lookup/doi/10.1101/2020.02.21.959627

612 55. Warren A, Chen Y, Jones A, Shibue T, Hahn WC, Boehm JS, et al. Global computational
613 alignment of tumor and cell line transcriptional profiles. Nat Commun. 2021;12:22.

614 56. Shi X, Gekas C, Verduzco D, Petiwala S, Jeffries C, Lu C, et al. Building a translational cancer
615 dependency map for The Cancer Genome Atlas. Nat Cancer. Nature Publishing Group;
616 2024;1–19.

617 57. Wang W, Albadari N, Du Y, Fowler JF, Sang HT, Xian W, et al. MDM2 Inhibitors for Cancer
618 Therapy: The Past, Present, and Future. Gottesman M, editor. Pharmacol Rev. 2024;76:414–
619 53.

620 58. Romero R, Sánchez-Rivera FJ, Westcott PMK, Mercer KL, Bhutkar A, Muir A, et al. Keap1
621 mutation renders lung adenocarcinomas dependent on Slc33a1. Nat Cancer. 2020;1:589–
622 602.

623 59. Ricketts CJ, De Cubas AA, Fan H, Smith CC, Lang M, Reznik E, et al. The Cancer Genome
624 Atlas Comprehensive Molecular Characterization of Renal Cell Carcinoma. Cell Rep.
625 2018;23:313-326.e5.

626 60. Gounder MM, Bauer TM, Schwartz GK, Weise AM, LoRusso P, Kumar P, et al. A First-in-
627 Human Phase I Study of Milademetan, an MDM2 Inhibitor, in Patients With Advanced
628 Liposarcoma, Solid Tumors, or Lymphomas. JCO. 2023;41:1714–24.

629 61. Drexler H, Fombonne S, Matsuo Y, Hu Z-B, Hamaguchi H, Uphoff C. p53 alterations in
630 human leukemia–lymphoma cell lines: in vitroartifact or prerequisite for cell
631 immortalization? Leukemia. 2000;14:198–206.

632 62. Achom M, Sadagopan A, Bao C, McBride F, Li J, Konda P, et al. A genetic basis for sex
633 differences in Xp11 translocation renal cell carcinoma. Cell [Internet]. Elsevier; 2024 [cited
634 2024 Aug 20];0. Available from: https://www.cell.com/cell/abstract/S0092-8674(24)00832-8

635 63. Maitituoheti M, Keung EZ, Tang M, Yan L, Alam H, Han G, et al. Enhancer Reprogramming
636 Confers Dependence on Glycolysis and IGF Signaling in KMT2D Mutant Melanoma. Cell Rep.
637 2020;33:108293.

638 64. Schoolmeester JK, Dao LN, Sukov WR, Wang L, Park KJ, Murali R, et al. TFE3 translocation-
639 associated perivascular epithelioid cell neoplasm (PEComa) of the gynecologic tract:
640 morphology, immunophenotype, differential diagnosis. Am J Surg Pathol. 2015;39:394–404.

641 65. Antonescu CR, Le Loarer F, Mosquera J-M, Sboner A, Zhang L, Chen C-L, et al. Novel YAP1-
642 TFE3 fusion defines a distinct subset of epithelioid hemangioendothelioma. Genes
643 Chromosomes Cancer. 2013;52:775–84.

644 66. Tanaka M, Chuaychob S, Homme M, Yamazaki Y, Lyu R, Yamashita K, et al. ASPSCR1::TFE3
645 orchestrates the angiogenic program of alveolar soft part sarcoma. Nat Commun.
646 2023;14:1957.

647 67. Wang X, Fang R, Zhang R, Ye S, Li R, Wang X, et al. Malignant melanotic Xp11 neoplasms
648 exhibit a clinicopathologic spectrum and gene expression profiling akin to alveolar soft part
649 sarcoma: a proposal for reclassification. J Pathol. 2020;251:365–77.

650 68. Lee SJ, Yang WI, Chung W-S, Kim SK. Epithelioid hemangioendotheliomas with TFE3 gene
651 translocations are compossible with CAMTA1 gene rearrangements. Oncotarget.
652 2016;7:7480–8.

653 69. Viswanathan VS, Ryan MJ, Dhruv HD, Gill S, Eichhoff OM, Seashore-Ludlow B, et al.
654 Dependency of a therapy-resistant state of cancer cells on a lipid peroxidase pathway.
655 Nature. 2017;547:453–7.

656 70. Caenepeel S, Karen R, Belmontes B, Verlinsky A, Tan H, Yang Y, et al. Abstract 6218:
657 Discovery and preclinical evaluation of AMG 397, a potent, selective and orally bioavailable
658 MCL1 inhibitor. Cancer Research. 2020;80:6218–6218.

659 71. Grubb T, Maganti S, Krill-Burger JM, Fraser C, Stransky L, Radivoyevitch T, et al. A
660 Mesenchymal Tumor Cell State Confers Increased Dependency on the BCL-XL Antiapoptotic
661 Protein in Kidney Cancer. Clin Cancer Res. 2022;28:4689–701.

662 72. Shakhova O, Zingg D, Schaefer SM, Hari L, Civenni G, Blunschi J, et al. Sox10 promotes the
663 formation and maintenance of giant congenital naevi and melanoma. Nat Cell Biol.
664 2012;14:882–90.

665 73. Cronin JC, Watkins-Chow DE, Incao A, Hasskamp JH, Schönewolf N, Aoude LG, et al. SOX10
666 ablation arrests cell cycle, induces senescence, and suppresses melanomagenesis. Cancer
667 Res. 2013;73:5709–18.

668 74. Morin PJ, Sparks AB, Korinek V, Barker N, Clevers H, Vogelstein B, et al. Activation of beta-
669 catenin-Tcf signaling in colon cancer by mutations in beta-catenin or APC. Science.
670 1997;275:1787–90.

671 75. Korinek V, Barker N, Morin PJ, van Wichen D, de Weger R, Kinzler KW, et al. Constitutive
672 transcriptional activation by a beta-catenin-Tcf complex in APC-/- colon carcinoma.
673 Science. 1997;275:1784–7.

674 76. Cancer Genome Atlas Network. Comprehensive molecular characterization of human colon
675 and rectal cancer. Nature. 2012;487:330–7.

676 77. Huang T, Hou Y, Wang X, Wang L, Yi C, Wang C, et al. Direct Interaction of Sox10 With
677 Cadherin-19 Mediates Early Sacral Neural Crest Cell Migration: Implications for Enteric
678 Nervous System Development Defects. Gastroenterology. 2022;162:179-192.e11.

679 78. Stamos JL, Weis WI. The β-catenin destruction complex. Cold Spring Harb Perspect Biol.
680 2013;5:a007898.

681 79. Kim J-S, Crooks H, Dracheva T, Nishanian TG, Singh B, Jen J, et al. Oncogenic beta-catenin is
682 required for bone morphogenetic protein 4 expression in human cancer cells. Cancer Res.
683 2002;62:2744–8.

684 80. Van Raay TJ, Fortino NJ, Miller BW, Ma H, Lau G, Li C, et al. Naked1 Antagonizes Wnt
685 Signaling by Preventing Nuclear Accumulation of β-Catenin. Koch K-W, editor. PLoS ONE.
686 2011;6:e18650.

687 81. Morrison L, Loibl S, Turner NC. The CDK4/6 inhibitor revolution — a game-changing era for
688 breast cancer treatment. Nat Rev Clin Oncol. 2024;21:89–105.

689 82. Ghandi M, Huang FW, Jané-Valbuena J, Kryukov GV, Lo CC, McDonald ER, et al. Next-
690 generation characterization of the Cancer Cell Line Encyclopedia. Nature. 2019;569:503–8.

691 83. Blache P, van de Wetering M, Duluc I, Domon C, Berta P, Freund J-N, et al. SOX9 is an
692 intestine crypt transcription factor, is regulated by the Wnt pathway, and represses the
693 CDX2 and MUC2 genes. J Cell Biol. 2004;166:37–47.

694 84. Kurnit KC, Sinno AK, Fellman BM, Varghese A, Stone R, Sood AK, et al. Effects of
695 Gastrointestinal-Type Chemotherapy in Women With Ovarian Mucinous Carcinoma. Obstet
696 Gynecol. 2019;134:1253–9.

697 85. Kurmasheva RT, Sammons M, Favours E, Wu J, Kurmashev D, Cosmopoulos K, et al. Initial
698 testing (stage 1) of tazemetostat (EPZ-6438), a novel EZH2 inhibitor, by the Pediatric
699 Preclinical Testing Program. Pediatr Blood Cancer. 2017;64.

700 86. Schmidt A, Behrendt L, Eybe J, Warmann SW, Schleicher S, Fuchs J, et al. The Effect of Direct
701 and Indirect EZH2 Inhibition in Rhabdomyosarcoma Cell Lines. Cancers (Basel). 2021;14:41.

702 87. Torchia J, Golbourn B, Feng S, Ho KC, Sin-Chan P, Vasiljevic A, et al. Integrated (epi)-
703 Genomic Analyses Identify Subgroup-Specific Therapeutic Targets in CNS Rhabdoid Tumors.
704 Cancer Cell. 2016;30:891–908.

705 88. Knutson SK, Warholic NM, Wigle TJ, Klaus CR, Allain CJ, Raimondi A, et al. Durable tumor
706 regression in genetically altered malignant rhabdoid tumors by inhibition of
707 methyltransferase EZH2. Proc Natl Acad Sci USA. 2013;110:7922–7.

708 89. Jones BA, Varambally S, Arend RC. Histone Methyltransferase EZH2: A Therapeutic Target for
709 Ovarian Cancer. Mol Cancer Ther. 2018;17:591–602.

710 90. Sasaki M, Kato D, Murakami K, Yoshida H, Takase S, Otsubo T, et al. Targeting dependency
711 on a paralog pair of CBP/p300 against de-repression of KREMEN2 in SMARCB1-deficient
712 cancers. Nat Commun. 2024;15:4770.

713 91. Voss MH, Chen D, Marker M, Hakimi AA, Lee C-H, Hsieh JJ, et al. Circulating biomarkers and
714 outcome from a randomised phase II trial of sunitinib vs everolimus for patients with
715 metastatic renal cell carcinoma. Br J Cancer. 2016;114:642–9.

716 92. Motzer RJ, Escudier B, McDermott DF, George S, Hammers HJ, Srinivas S, et al. Nivolumab
717 versus Everolimus in Advanced Renal-Cell Carcinoma. N Engl J Med. 2015;373:1803–13.

718 93. Sinha R, Winer AG, Chevinsky M, Jakubowski C, Chen Y-B, Dong Y, et al. Analysis of renal
719 cancer cell lines from two major resources enables genomics-guided cell line selection. Nat
720 Commun. Nature Publishing Group; 2017;8:15165.

721 94. Bakouny Z, Braun DA, Shukla SA, Pan W, Gao X, Hou Y, et al. Integrative molecular
722 characterization of sarcomatoid and rhabdoid renal cell carcinoma. Nature
723 Communications. Nature Publishing Group; 2021;12:808.

724 95. Maughan BL, Sirohi D. Papillary Renal Cell Carcinoma: A Review of Prospective Clinical
725 Trials. Curr Treat Options in Oncol. 2023;24:1199–212.

726 96. Henske EP, Cheng L, Hakimi AA, Choueiri TK, Braun DA. Chromophobe renal cell carcinoma.
727 Cancer Cell. 2023;41:1383–8.

728 97. Bártů M, Hojný J, Hájková N, Michálková R, Krkavcová E, Hadravský L, et al. Analysis of
729 expression, epigenetic, and genetic changes of HNF1B in 130 kidney tumours. Sci Rep.
730 2020;10:17151.

731 98. Wang C-C, Mao T-L, Yang W-C, Jeng Y-M. Underexpression of hepatocyte nuclear factor-1β
732 in chromophobe renal cell carcinoma. Histopathology. 2013;62:589–94.

733 99. Kalev P, Hyer ML, Gross S, Konteatis Z, Chen C-C, Fletcher M, et al. MAT2A Inhibition Blocks
734 the Growth of MTAP-Deleted Cancer Cells by Reducing PRMT5-Dependent mRNA Splicing
735 and Inducing DNA Damage. Cancer Cell. 2021;39:209-224.e11.

736 100. Adam J, Hatipoglu E, O'Flaherty L, Ternette N, Sahgal N, Lockstone H, et al. Renal cyst
737 formation in Fh1-deficient mice is independent of the Hif/Phd pathway: roles for fumarate in
738 KEAP1 succination and Nrf2 signaling. Cancer Cell. 2011;20:524–37.

739 101. Chen F, Zhang Y, Şenbabaoğlu Y, Ciriello G, Yang L, Reznik E, et al. Multilevel Genomics-
740 Based Taxonomy of Renal Cell Carcinoma. Cell Reports. 2016;14:2476–89.

741 102. Fabrizio FP, Costantini M, Copetti M, la Torre A, Sparaneo A, Fontana A, et al. Keap1/Nrf2
742 pathway in kidney cancer: frequent methylation of KEAP1 gene promoter in clear renal cell
743 carcinoma. Oncotarget. 2017;8:11187–98.

744 103. Pillai R, Hayashi M, Zavitsanou A-M, Papagiannakopoulos T. NRF2: KEAPing Tumors
745 Protected. Cancer Discovery. 2022;12:625–43.

746 104. M G, T P, L B-P. Reductive stress in cancer: coming out of the shadows. Trends in cancer
747 [Internet]. Trends Cancer; 2024 [cited 2024 Feb 28];10. Available from:
748 https://pubmed.ncbi.nlm.nih.gov/37925319/

749 105. Weiss-Sadan T, Ge M, Hayashi M, Gohar M, Yao C-H, de Groot A, et al. NRF2 activation
750 induces NADH-reductive stress, providing a metabolic vulnerability in lung cancer. Cell
751 Metabolism. 2023;S1550413123000128.

752 106. Köferle A, Schlattl A, Hörmann A, Thatikonda V, Popa A, Spreitzer F, et al. Interrogation of
753 cancer gene dependencies reveals paralog interactions of autosome and sex chromosome-
754 encoded genes. Cell Rep. 2022;39:110636.

755 107. Qi M, Pang J, Mitsiades I, Lane AA, Rheinbay E. Loss of chromosome Y in primary tumors.
756 Cell. 2023;S0092-8674(23)00646-3.

757 108. Donehower LA, Soussi T, Korkut A, Liu Y, Schultz A, Cardenas M, et al. Integrated Analysis of
758 TP53 Gene and Pathway Alterations in The Cancer Genome Atlas. Cell Rep. 2019;28:1370-
759 1384.e5.

760 109. Zou Y, Palte MJ, Deik AA, Li H, Eaton JK, Wang W, et al. A GPX4-dependent cancer cell state
761 underlies the clear-cell morphology and confers sensitivity to ferroptosis. Nat Commun.
762 Nature Publishing Group; 2019;10:1617.

763 110. Steingrímsson E, Tessarollo L, Pathak B, Hou L, Arnheiter H, Copeland NG, et al. Mitf and
764 Tfe3, two members of the Mitf-Tfe family of bHLH-Zip transcription factors, have important
765 but functionally redundant roles in osteoclast development. PNAS. National Academy of
766 Sciences; 2002;99:4477–82.

767 111. Pastore N, Vainshtein A, Klisch TJ, Armani A, Huynh T, Herz NJ, et al. TFE3 regulates whole-
768 body energy metabolism in cooperation with TFEB. EMBO Mol Med. 2017;9:605–21.

769 112. Settembre C, De Cegli R, Mansueto G, Saha PK, Vetrini F, Visvikis O, et al. TFEB controls
770 cellular lipid metabolism through a starvation-induced autoregulatory loop. Nat Cell Biol.
771 2013;15:647–58.

772 113. Raben N, Puertollano R. TFEB and TFE3: Linking Lysosomes to Cellular Adaptation to Stress.
773 Annu Rev Cell Dev Biol. 2016;32:255–78.

774 114. Chiu Y-C, Zheng S, Wang L-J, Iskra BS, Rao MK, Houghton PJ, et al. Predicting and
775 characterizing a cancer dependency map of tumors with deep learning. Sci Adv.
776 2021;7:eabh1275.

777 115. Yuda J, Will C, Phillips DC, Abraham L, Alvey C, Avigdor A, et al. Selective MCL-1 inhibitor
778 ABBV-467 is efficacious in tumor models but is associated with cardiac troponin increases
779 in patients. Commun Med. 2023;3:154.

780 116. Rauh U, Wei G, Serrano-Wu M, Kosmidis G, Kaulfuss S, Siegel F, et al. BRD-810 is a highly
781 selective MCL1 inhibitor with optimized in vivo clearance and robust efficacy in solid and
782 hematological tumor models. Nat Cancer [Internet]. 2024 [cited 2024 Sep 5]; Available from:
783 https://www.nature.com/articles/s43018-024-00814-0

784 117. Msaouel P, Genovese G, Tannir NM. Renal Cell Carcinoma of Variant Histology: Biology and
785 Therapies. Hematol Oncol Clin North Am. 2023;S0889-8588(23)00053-9.

786 118. Msaouel P, Malouf GG, Su X, Yao H, Tripathi DN, Soeung M, et al. Comprehensive Molecular
787 Characterization Identifies Distinct Genomic and Immune Hallmarks of Renal Medullary
788 Carcinoma. Cancer Cell. 2020;37:720-734.e13.

789 119. Coutinho DF, Mundi PS, Marks LJ, Burke C, Ortiz MV, Diolaiti D, et al. Validation of a non-
790 oncogene encoded vulnerability to exportin 1 inhibition in pediatric renal tumors. Med.
791 2022;3:774-791.e7.

792 120. Wang J, Papanicolau-Sengos A, Chintala S, Wei L, Liu B, Hu Q, et al. Collecting duct
793 carcinoma of the kidney is associated with CDKN2A deletion and SLC family gene up-
794 regulation. Oncotarget. 2016;7:29901–15.

795 121. Doench JG, Hartenian E, Graham DB, Tothova Z, Hegde M, Smith I, et al. Rational design of
796 highly active sgRNAs for CRISPR-Cas9–mediated gene inactivation. Nat Biotechnol.
797 2014;32:1262–7.

798 122. Doench JG, Fusi N, Sullender M, Hegde M, Vaimberg EW, Donovan KF, et al. Optimized
799 sgRNA design to maximize activity and minimize off-target effects of CRISPR-Cas9. Nat
800 Biotechnol. 2016;34:184–91.

801 123. Sanson KR, Hanna RE, Hegde M, Donovan KF, Strand C, Sullender ME, et al. Optimized
802 libraries for CRISPR-Cas9 genetic screens with multiple modalities. Nat Commun.
803 2018;9:5416.

804 124. Shalem O, Sanjana NE, Hartenian E, Shi X, Scott DA, Mikkelsen TS, et al. Genome-Scale
805 CRISPR-Cas9 Knockout Screening in Human Cells. Science. 2014;343:84–7.

806 125. Sanjana NE, Shalem O, Zhang F. Improved vectors and genome-wide libraries for CRISPR
807 screening. Nat Methods. 2014;11:783–4.

808 126. Li W, Xu H, Xiao T, Cong L, Love MI, Zhang F, et al. MAGeCK enables robust identification of
809 essential genes from genome-scale CRISPR/Cas9 knockout screens. Genome Biol.
810 2014;15:554.

811 127. Li H, Durbin R. Fast and accurate short read alignment with Burrows-Wheeler transform.
812 Bioinformatics. 2009;25:1754–60.

813 128. Riester M, Singh AP, Brannon AR, Yu K, Campbell CD, Chiang DY, et al. PureCN: copy
814 number calling and SNV classification using targeted short read sequencing. Source Code
815 Biol Med. 2016;11:13.

816 129. Li B, Dewey CN. RSEM: accurate transcript quantification from RNA-Seq data with or without
817 a reference genome. BMC Bioinformatics. 2011;12:323.

818 130. Dobin A, Davis CA, Schlesinger F, Drenkow J, Zaleski C, Jha S, et al. STAR: ultrafast universal
819 RNA-seq aligner. Bioinformatics. 2013;29:15–21.

820 131. Tatlow PJ, Piccolo SR. A cloud-based workflow to quantify transcript-expression levels in
821 public cancer compendia. Sci Rep. 2016;6:39259.

822 132. Zhang Y, Parmigiani G, Johnson WE. ComBat-seq: batch effect adjustment for RNA-seq
823 count data. NAR Genom Bioinform. 2020;2:lqaa078.

133. Braun DA, Hou Y, Bakouny Z, Ficial M, Sant' Angelo M, Forman J, et al. Interplay of somatic alterations and immune infiltration modulates response to PD-1 blockade in advanced clear cell renal cell carcinoma. Nat Med. Nature Publishing Group; 2020;26:909–18.

134. Davidson-Pilon C. lifelines: survival analysis in Python. Journal of Open Source Software. 2019;4:1317.

135. Seavey CN, Pobbati AV, Hallett A, Ma S, Reynolds JP, Kanai R, et al. WWTR1(TAZ)-CAMTA1 gene fusion is sufficient to dysregulate YAP/TAZ signaling and drive epithelioid hemangioendothelioma tumorigenesis. Genes Dev. 2021;35:512–27.

136. Braun DA, Ishii Y, Walsh AM, Van Allen EM, Wu CJ, Shukla SA, et al. Clinical Validation of *PBRM1* Alterations as a Marker of Immune Checkpoint Inhibitor Response in Renal Cell Carcinoma. JAMA Oncol. 2019;5:1631.

137. Motzer RJ, Tannir NM, McDermott DF, Arén Frontera O, Melichar B, Choueiri TK, et al. Nivolumab plus Ipilimumab versus Sunitinib in Advanced Renal-Cell Carcinoma. N Engl J Med. 2018;378:1277–90.

138. Cancer Genome Atlas Research Network, Weinstein JN, Collisson EA, Mills GB, Shaw KRM, Ozenberger BA, et al. The Cancer Genome Atlas Pan-Cancer analysis project. Nat Genet. 2013;45:1113–20.

139. Cancer Genome Atlas Research Network, Linehan WM, Spellman PT, Ricketts CJ, Creighton CJ, Fei SS, et al. Comprehensive Molecular Characterization of Papillary Renal-Cell Carcinoma. N Engl J Med. 2016;374:135–45.

140. Davis CF, Ricketts CJ, Wang M, Yang L, Cherniack AD, Shen H, et al. The somatic genomic landscape of chromophobe renal cell carcinoma. Cancer Cell. 2014;26:319–30.

141. Liu YJ, Ussakli C, Antic T, Liu Y, Wu Y, True L, et al. Sporadic oncocytic tumors with features intermediate between oncocytoma and chromophobe renal cell carcinoma: comprehensive clinicopathological and genomic profiling. Hum Pathol. 2020;104:18–29.

Acknowledgements:

Schematic illustrations were created with BioRender.com.

Funding: S.R.V: Doris Duke Charitable Foundation (Clinician-Scientist Development Award grant number: 2020101), Department of Defense Kidney Cancer Research Program (DoD KCRP) (W81XWH-19-1-0815 / KC180130; W81XWH-22-1-1016 / KC210039), NCI (R01CA286652; R01CA279044; R01CA269505), DF/HCC Kidney SPORE (2P50CA101942-16), Rally Foundation Independent Investigator Grant (23IN3). J.L.: Department of Defense Kidney Cancer Research Program (DoD KCRP) (W81XWH-22-1-0399). P.K. Department of Defense Kidney Cancer Research Program (DoD KCRP) Postdoctoral and Clinical Fellowship (HT94252310066). C.N.W.: American Association for Cancer Research (AACR) Exelixis Renal Cell Carcinoma Research Fellowship (1306525). T.K.C.: Dana-Farber/Harvard Cancer Center Kidney SPORE (2P50CA101942-16) and Program 5P30CA00651656, the Kohlberg Chair at Harvard Medical School and the Trust Family, Michael Brigham, Pan Mass Challenge, Hinda and Arthur Marcus Fund, and Loker Pinard Funds for Kidney Cancer Research at DFCI.

Author contributions: S.R.V designed and supervised the study. B.L., A.S., S.R.V wrote the manuscript with input from all co-authors. A.S. performed analysis of genome-scale CRISPR screening data, dependency prediction and developed the predictive model used in this study. Y.C. and P.K. assisted in analysis of dependency data. B.L. led experimental work including genome-scale CRISPR screening and dependency validation. J.L., C.N.W., Y.W. assisted in experimental work and contributed to experimental design. T.K.C., A.S., provided clinical trial data and/or analysis. J.G.D. contributed to design of screening and validation studies.

Data Availability: Chronos scores from tRCC CRISPR screen are available in **Supplementary Table S1.** External datasets analyzed are public and are available from the respective cited publications. Chronos score predictions for all external datasets are available in **Supplementary Table S4.**

Code Availability: Code for the developed tool will be publicly available in Github at time of publication: https://github.com/SViswanathanLab/TrPLet.

Declaration of Interests: Aspects of this work are the subject of a pending patent application (A.S., S.R.V.). S.R.V.: has consulted for Jnana Therapeutics within the past 3 years; receives research support from Bayer. T.K.C. reports institutional and personal paid or unpaid support for research, advisory board participation, consultancy, and honoraria within the past 5 years from Alkermes, Arcus Bio, AstraZeneca, Aravive, Aveo, Bayer, Bristol Myers Squibb, Calithera, Circle Pharma, Deciphera Pharmaceuticals, Eisai, EMD Serono, Exelixis, GlaxoSmithKline, Gilead, HiberCell, IQVIA, Infinity, Ipsen, Jansen, Kanaph, Lilly, Merck, Nikang, Neomorph, Nuscan and Precede Bio, Novartis, Oncohost, Pfizer, Roche, Sanofi Aventis, Scholar Rock, Surface Oncology, Takeda, and Tempest and equity in Tempest, Pionyr, Osel, Precede Bio, CureResponse, InnDura Therapeutics, and Primium.

List of Supplementary Materials

Materials and Methods
Supplementary Fig. S1 to Fig. S6
Supplementary Table S1 to Table S4
References 125-145

Main Figures and Captions

Fig.1 | Genome-scale genetic screening reveals selective essentialities of tRCC cells

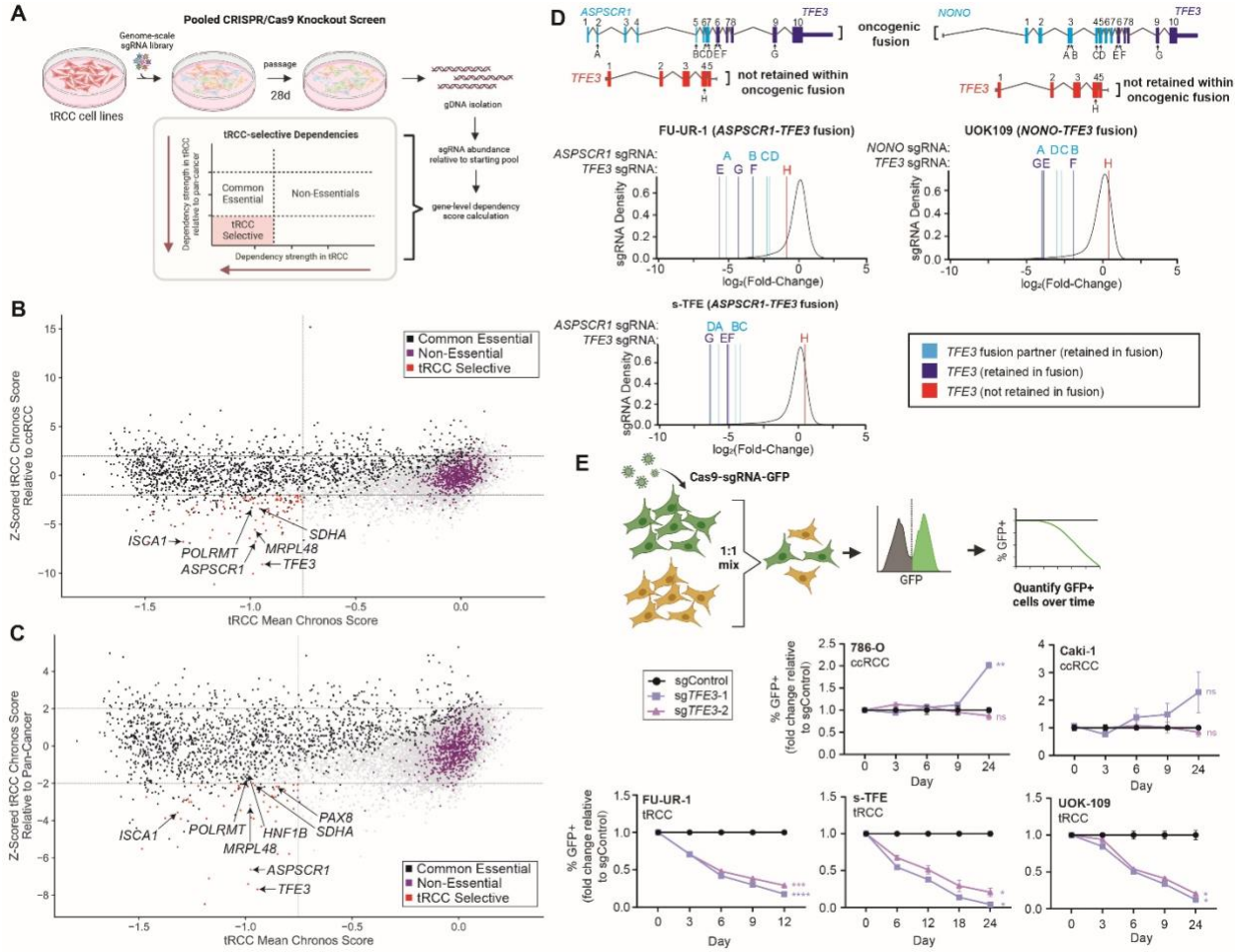

(A) Workflow for CRISPR screens and analysis to identify tRCC-selective genetic dependencies.

(B-C) Landscape of tRCC-selective dependencies. Mean Chronos score for each gene across the 3 tRCC cell lines screened in this study is plotted against the Z-scored Chronos score for that gene (Z-score calculated relative to DepMap ccRCC cell lines in **B** and relative to all DepMap cell lines in **C**). Non-essential-genes are colored in purple while common essential genes are colored in black (42). tRCC-selective dependencies (defined as Z-score < -2; absolute Chronos score < -0.75) are colored in red.

(D) Log-fold change for individual sgRNAs targeting either *TFE3* (E, F, G, H) or fusion partner (A, B, C, D) in tRCC CRISPR screens. The exons targeted by each sgRNA are indicated in the schematics. For each cell line, the top schematic represents the exons coding for the oncogenic fusion while the bottom schematic represents the N-terminal exons of *TFE3* not included in the oncogenic fusion. Density plot shows the distribution for LFC of all sgRNAs assessed in the CRISPR screen in each cell line while vertical lines represent log-fold change for individual sgRNAs. Note: Figure shows the *ASPSCR1-TFE3* fusion in s-TFE cells; the *ASPSCR1-TFE3* fusion in FU-UR-1 cells retains exon 5 of *TFE3* exon 5.

(E) Competitive growth assay to assess the effects of *TFE3* knockout in two ccRCC lines (786-O, Caki-1) and three tRCC lines (UOK109, FU-UR-1, s-TFE). Cells expressing Cas9/sgRNA and GFP were mixed in a 1:1 ratio

910 with parental cells and proportion relative to sgControl cells was calculated at each time point via flow
911 cytometry. Shown as mean +/- s.d., n=2 biological replicates per condition. *P*-values were calculated by
912 Welch's (two-tailed unpaired) t-test as compared with sgControl samples at the final time point. *$P < 0.05$, **P
913 < 0.01, ***$P < 0.001$, ****$P < 0.0001$.

914

Fig.2 | Validation of selective tRCC dependencies

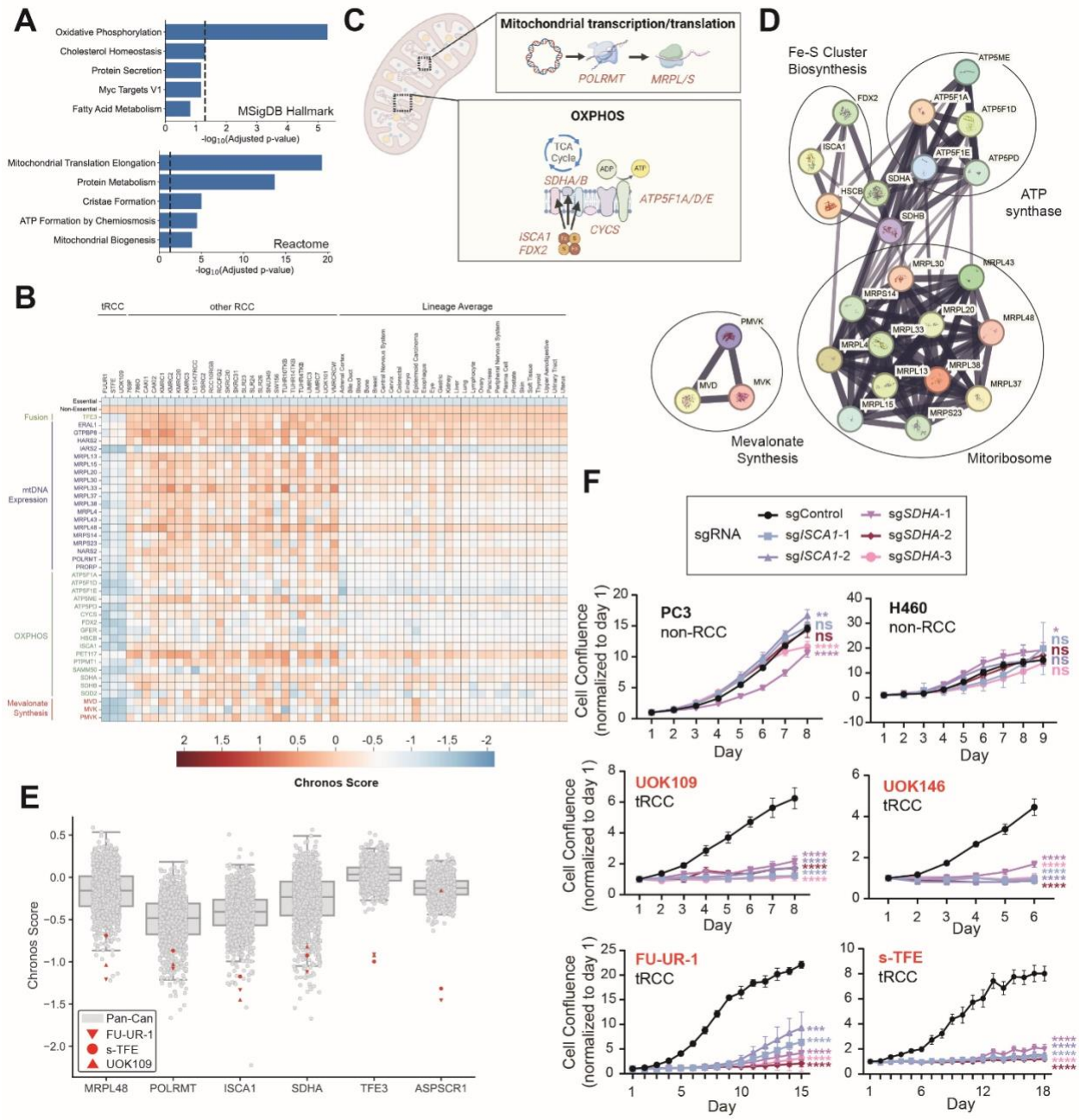

(A) Pathway enrichment (Enrichr) on gene dependencies shared across all three tRCC cell lines (defined as genes with ΔChronos ≤ -0.5 between every tRCC cell line and DepMap ccRCC mean).

(B) Heat map of tRCC-selective dependencies (defined as genes with ΔChronos ≤ -0.5 between every tRCC cell line and DepMap ccRCC mean), for selected pathways (remaining genes/pathways shown in **Supplementary Fig. S1B**). Chronos scores for individual tRCC cell lines, DepMap RCC cell lines, and average Chronos score for each of 28 lineages screened in DepMap are shown. The top two rows indicate mean Chronos scores for essential and non-essential genes in each column, shown for reference.

925 **(C)** Schematic depicting tRCC-selective dependencies that fall within pathways related to mitochondrial
926 metabolism.

927 **(D)** Protein-protein interaction network amongst interacting tRCC-selective gene dependencies (genes with
928 ΔChronos ≤ -0.5 between every tRCC cell line and DepMap ccRCC mean) involved in mtDNA expression,
929 OXPHOS, and mevalonate synthesis (STRINGdb).

930 **(E)** Distribution of Chronos scores for indicated genes (*POLRMT*, *MRPL48*, *ISCA1, SDHA, TFE3, ASPSCR1*)
931 across all DepMap cell lines (gray) and tRCC cell lines screened in this study (red).

932 **(F)** Relative confluence of non-RCC cells (PC3, H460), and tRCC cells (UOK109, UOK146, FU-UR-1, s-TFE) after
933 infection with lentivirus expressing Cas9 and either non-targeting control sgRNA, *ISCA1* sgRNAs, or *SDHA*
934 sgRNAs. Confluence was normalized to day 1, shown as mean +/- s.d., n=6 biological replicates per condition.
935 *P*-values were calculated by Welch's (two-tailed unpaired) t test as compared with sgControl samples for the
936 last assay day. *$P < 0.05$, **$P < 0.01$, ***$P < 0.001$, ****$P < 0.0001$.

937

Fig.3 | A machine-learning model uncovers additional strong dependencies in tRCC subsets

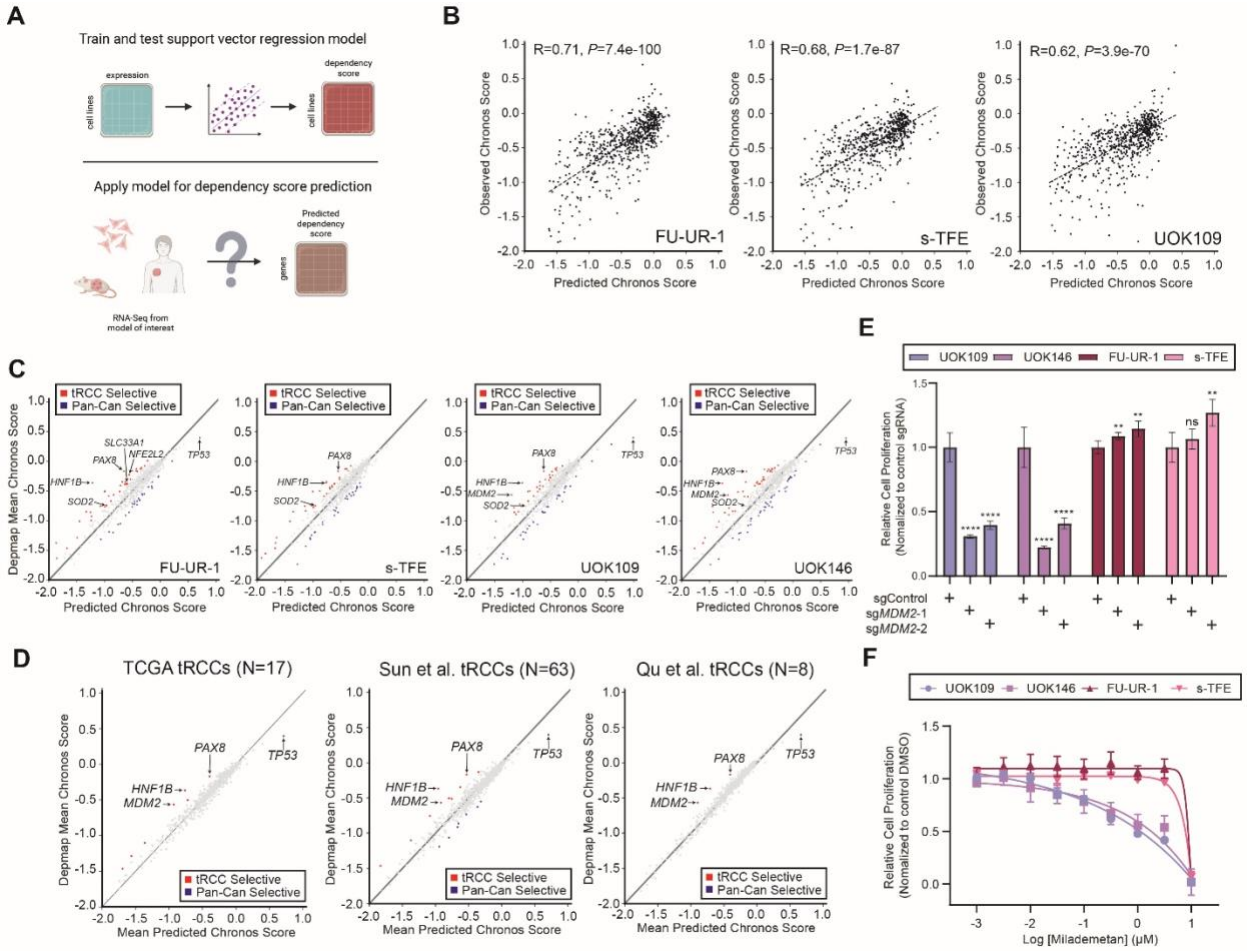

(A) Schematic of machine learning approach used to nominate candidate vulnerabilities in cell lines or tumors based on RNA-Seq profile.

(B) Correlation between observed Chronos score from CRISPR screen performed in this study and Chronos score predicted by our model, for 645 dependencies across three tRCC cell lines (FU-UR-1, S-TFE, UOK109; *Note*: discrepancy in number of genes predicted (N=657) and plotted (N=645) due to imperfect overlap in genes screened between Avana [DepMap] and Brunello libraries [tRCC screen]). *P*-values calculated from Pearson's correlation test.

(C) tRCC-selective dependencies based on predicted Chronos scores across four tRCC cell lines, including one line (UOK146) that was not assessed by genome-scale CRISPR screening. In each cell line, predicted Chronos scores in the tRCC cell line are plotted against mean Chronos score across all DepMap cell lines (as experimentally determined by genome-scale CRISPR screening). Red: ΔChronos ≤ -0.2; blue: ΔChronos ≥ 0.2 between predicted and DepMap mean.

(D) tRCC-selective dependencies based on mean predicted Chronos scores for 657 genes across tRCC tumors in three independent cohorts, as compared with mean Chronos score across all DepMap cell lines (red: ΔChronos ≤ -0.2; blue: ΔChronos ≥ 0.2 between mean predicted and DepMap mean Chronos scores).

956 **(E)** Relative viability of tRCC cells (UOK109, UOK146, FU-UR-1, s-TFE) after CRISPR/Cas9 knockout of *MDM2*.
957 Viability is normalized to control sgRNA, shown as mean +/- s.d., n=6 biological replicates per condition. *P*-
958 values were calculated by Welch's (two-tailed unpaired) t test as compared with sgControl samples. *$P < 0.05$,
959 **$P < 0.01$, ***$P < 0.001$, ****$P < 0.0001$.

960 **(F)** Viability of tRCC cell lines treated with indicated concentrations of milademetan (MDM2 inhibitor) and
961 assayed for cell viability after 3 days with CellTiter-Glo. Viability at each concentration is relative to vehicle-
962 treated cells, shown as mean +/- s.d., n=6 biological replicates.

963

964 **Fig.4 | Predicting and validating dependencies in ASPS**

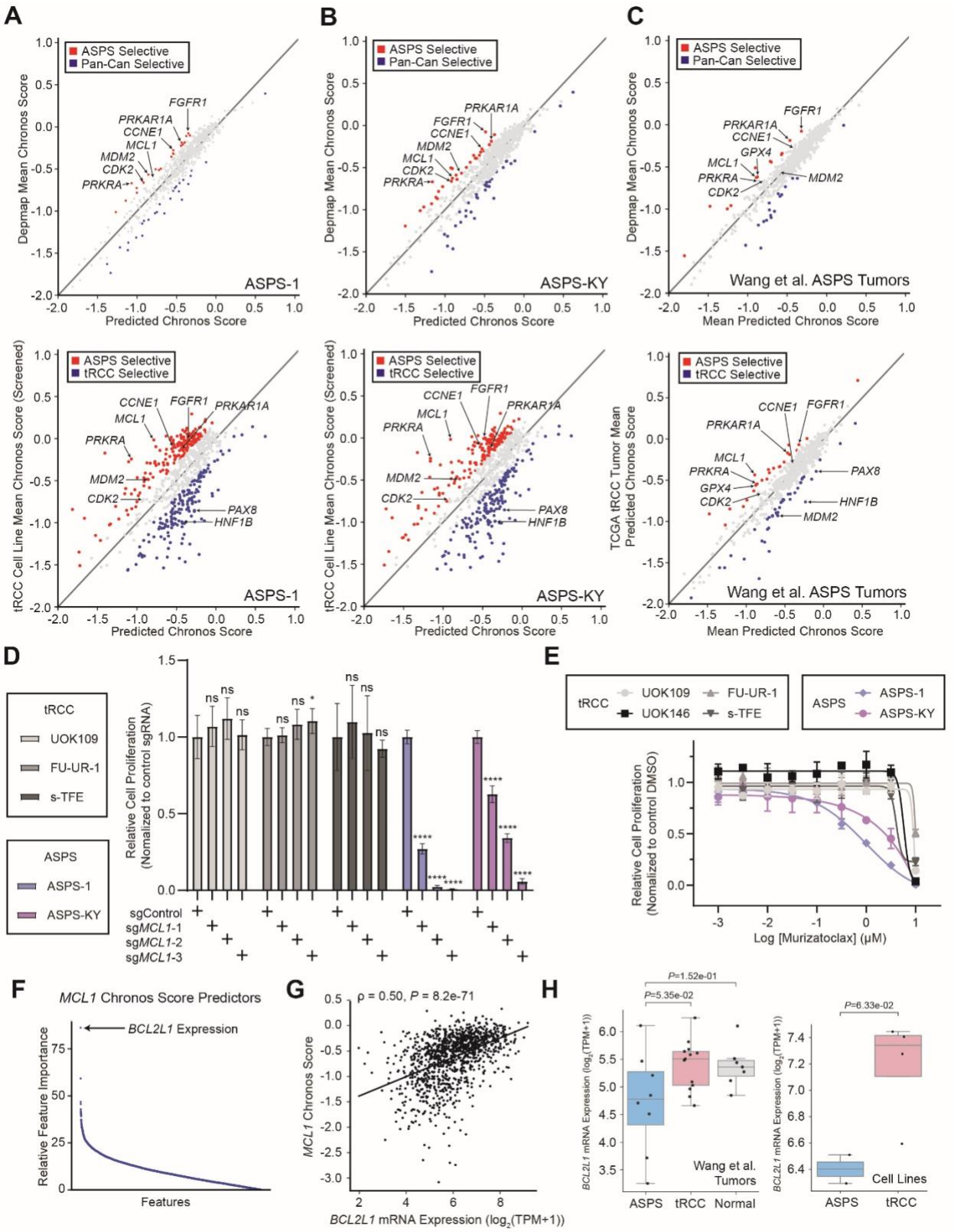

965

966

967 **(A-C)** Selective dependencies in ASPS cell lines(ASPS-1 **(A)**, ASPS-KY **(B)**) or ASPS tumors (**(C)**, profiled by
968 RNA-Seq in a prior study (67)) based on their (mean) predicted Chronos scores as compared with mean
969 Chronos score across all DepMap cell lines (top panels) or tRCC cell lines/TCGA tRCC tumors that were
970 screened/predicted in this study (bottom panels). Red: ΔChronos ≤ -0.2; blue: ΔChronos ≥ 0.2 between
971 (mean) predicted Chronos score and DepMap mean (top) or tRCC cell line/TCGA tRCC tumor mean (bottom).

972 **(D)** Proliferation of ASPS cell lines transduced with one of 3 distinct sgRNAs targeting *MCL1* or a non-targeting
973 sgRNA control. Shown as mean +/- s.d., n = 6 biological replicates per condition. *P*-values were calculated by
974 Welch's t-test (two-tailed unpaired) as compared with sgControl samples. *$P < 0.05$, **$P < 0.01$, ***$P <$
975 0.001, ****$P < 0.0001$.

976 **(E)** Viability of ASPS-1 and ASPS-KY and non-ASPS (versus tRCC) cell lines treated with indicated
977 concentrations of murizatoclax (MCL1 inhibitor) and assayed for cell viability after 3 days with CellTiter-Glo.
978 Viability at each concentration is relative to vehicle-treated cells, shown as mean +/- s.d., n=3 replicates.

979 **(F)** Relative feature importance (ranked across top 5000 features) for RNA predictors of *MCL1* Chronos score.
980 Each point represents an individual feature (see **Methods**).

981 **(G)** *MCL1* Chronos score is plotted against *BCL2L1* mRNA expression ($\log_2$(TPM+1)) across all DepMap cell
982 lines.

983 **(H)** *BCL2L1* mRNA expression ($\log_2$(TPM+1)) in ASPS tumors, tRCC tumors, and kidney-adjacent normal
984 tissue from Wang et al. (67) (left) as well as ASPS cell lines (ASPS-1, ASPS-KY) and tRCC cell lines (FU-UR-1,
985 s-TFE, UOK109, UOK146) (right) profiled by RNA-seq are shown. *P*-values computed by Welch's (two-tailed
986 unpaired) t-test.

987

988 **Fig.5 | A landscape of candidate dependencies across TCGA**

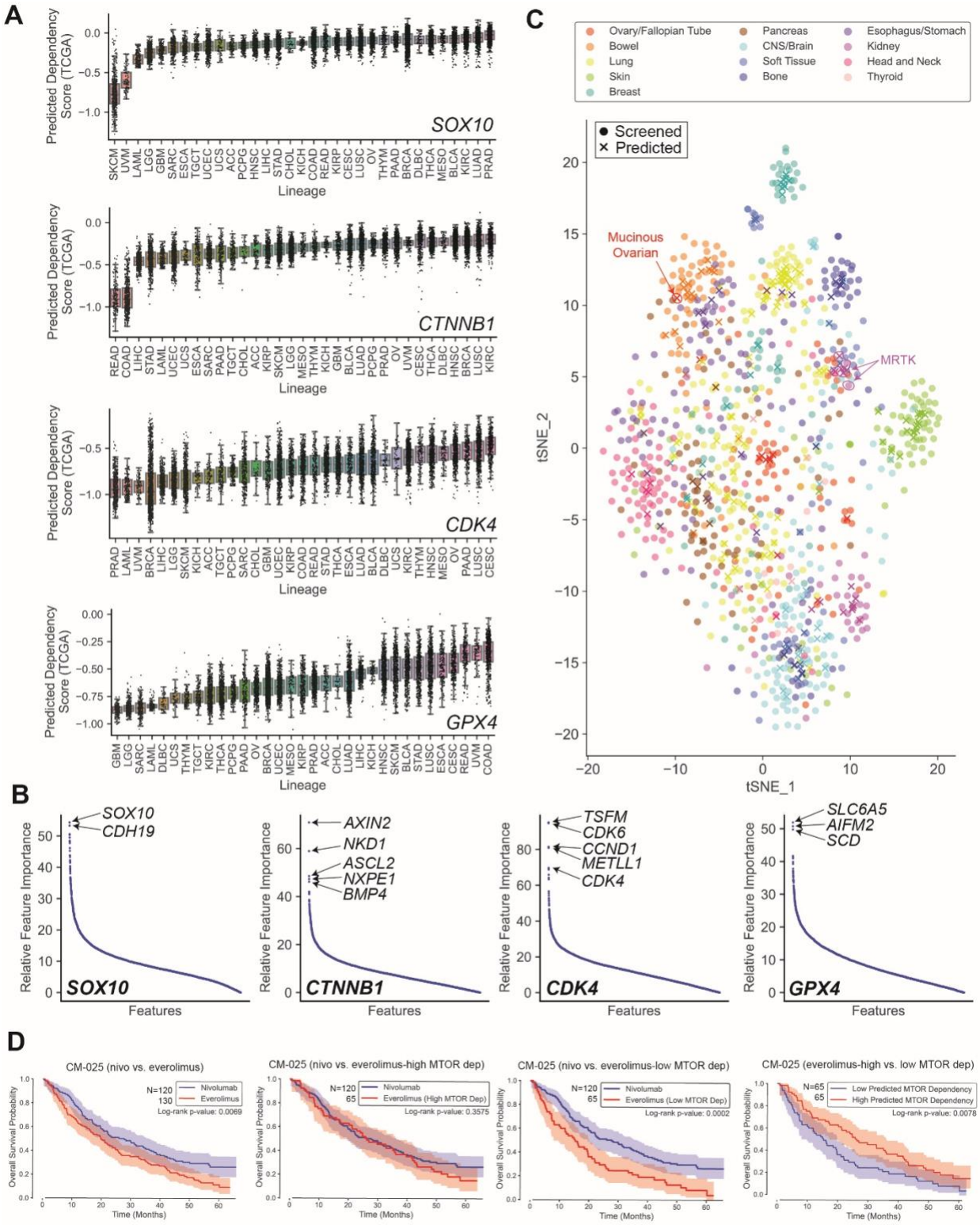

989

990

991 **(A)** Predicted Chronos scores for *SOX10*, *CTNNB1*, *CDK4* and *GPX*4 across tumor types profiled in TCGA;
992 tumors grouped by TCGA lineage.
993 **(B)** Relative feature importance (ranked across top 5000 features) for RNA predictors of *SOX10*, *CTNNB1*,
994 *CDK4* and *GPX*4 Chronos scores. Each point represents an individual feature (see **Methods**).
995 **(C)** *t*-SNE projection based on dependency score for cell lines experimentally screened in the DepMap
996 (N=833, circle) or cell lines for which dependencies for 657 PD genes were predicted by our model (N=251
997 cell lines, cross). Cell lines are colored based on annotated lineage, with 13 common lineages plotted
998 (lineages with ≥10 predicted cell lines; hematological lineages and fibroblasts removed). Selected cell lines
999 whose dependency predictions diverge from the parental lineage are highlighted.
1000 **(D)** Overall survival (OS) for ccRCC patients on clinical trial of nivolumab vs. everolimus (CM-025). From left
1001 to right: nivolumab vs. everolimus in the overall population; nivolumab vs. everolimus-treated patients with
1002 high predicted *MTOR* dependency; nivolumab vs. everolimus-treated patients with low predicted *MTOR*
1003 dependency; everolimus-treated patients with high vs. low predicted *MTOR* dependency. *P*-values
1004 calculated by log-rank test.
1005

1006 **Fig.6 | A landscape of candidate dependencies across rare kidney cancers**

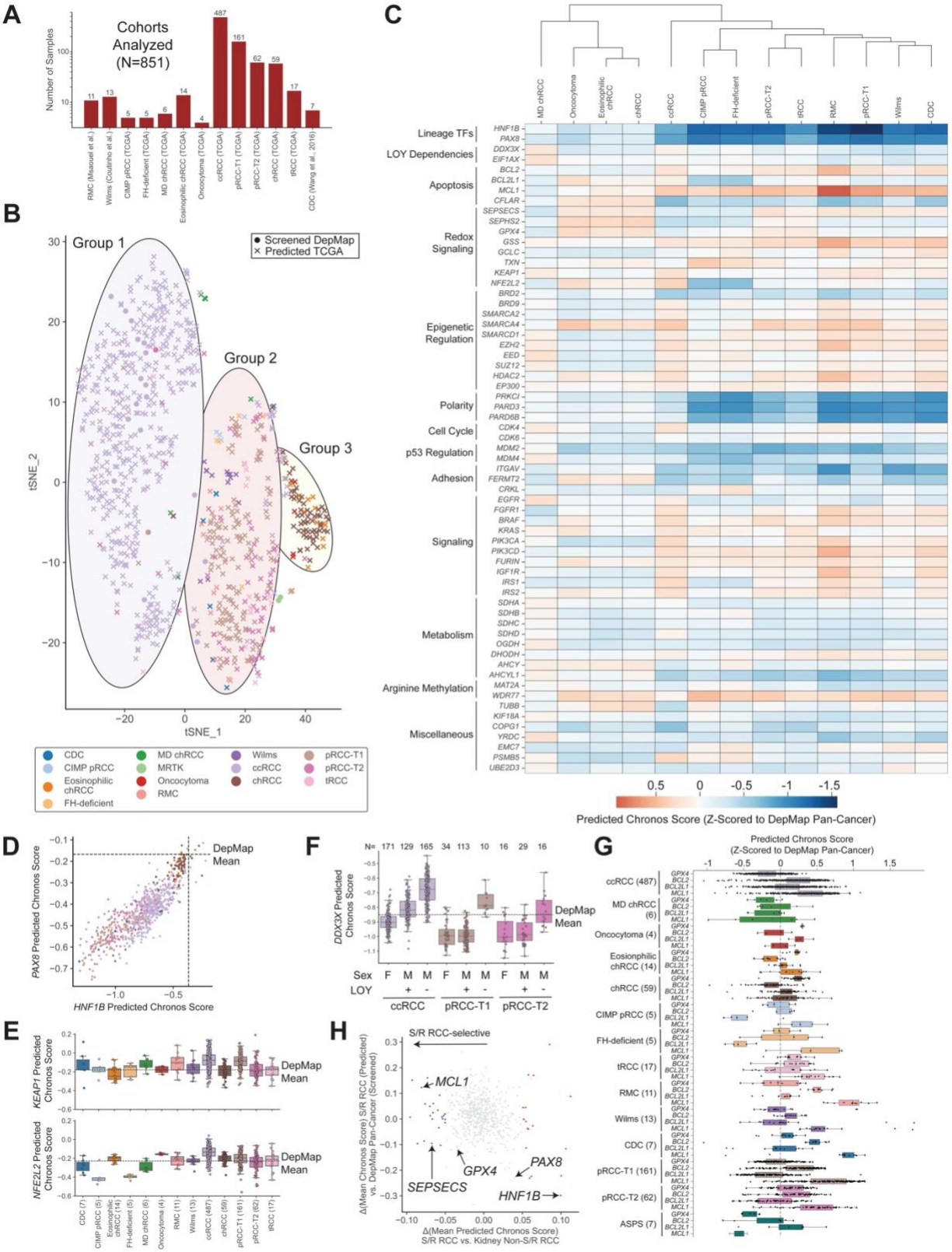

1007

1008 **(A)** RNA-Seq data from 851 renal tumor-derived samples was curated from across 4 published datasets
1009 (59,118–120), representing 13 distinct types of kidney cancer. The number of samples for each kidney cancer
1010 subtype is shown.

1011 **(B)** *t*-SNE projection based on dependency score for kidney tumors with dependencies predicted by our model
1012 (N=851, cross) and kidney cancer cell lines experimentally screened in the DepMap (N=22), across 657 PD
1013 genes. Tumors are colored based on annotated subtype and three groups are outlined.

1014 **(C)** Heatmap of predicted Chronos score (Z-scored to DepMap pan-cancer value for screened cell lines) for
1015 63 curated dependencies, including those selective in one or more subtypes of kidney cancer (relative to
1016 pan-cancer) or additional actionable dependencies with small molecule inhibitors. Individual kidney tumor
1017 subtypes are as in **Fig.6A-B**. Hierarchical clustering is based on genes shown in the heatmap.

1018 **(D)** Scatter plot of predicted *HNF1B* Chronos score versus predicted *PAX8* Chronos score for individual
1019 kidney tumors (N=851), colored by subtype as indicated in **Fig.6B**. DepMap mean Chronos score for each of
1020 these genes across experimentally screened cell lines is indicated by dotted lines.

1021 **(E)** Box plot of predicted *KEAP1* (top) and *NFE2L2* (bottom) Chronos score for individual kidney tumors
1022 (N=851), grouped by subtype indicated in **Fig.6A-B**. Mean Chronos score in DepMap (experimentally derived)
1023 for these genes are indicated by dotted lines. All box plots are shown with median, upper and lower quartile
1024 lines, and extend to [Q1-1.5xIQR, Q3+1.5xIQR].

1025 **(F)** Box plot of predicted *DDX3X* Chronos score across ccRCC, pRCC-T1, and pRCC-T2 tumors in TCGA
1026 stratified by annotated sex and loss of chrY (LOY) status (107). Experimentally derived mean Chronos score
1027 for *DDX3X* in DepMap is indicated as a dotted line.

1028 **(G)** Box plot of predicted *GPX4*, *BCL2*, *BCL2L1*, and *MCL1* Chronos score (Z-scored to DepMap pan-cancer)
1029 for individual kidney tumors (N=851), grouped by subtype indicated in **Fig.6A**. DepMap mean (Z=0) is
1030 indicated as a dotted line. Predictions for ASPS, which was experimentally confirmed to be *MCL1* dependent
1031 (**Fig.4**) are also shown as reference.

1032 **(H)** Predicted dependency scores for S/R RCCs vs. non-S/R RCCs (ccRCC, pRCC-T1, pRCC-T2, chRCC) in
1033 TCGA (94). Difference in mean predicted Chronos score between S/R RCCs and non-S/R RCCs is plotted
1034 against the difference in mean Chronos score between S/R RCCs (predicted) and the DepMap pan-cancer
1035 mean. Points are colored based on the comparison between S/R RCCs and non-S/R RCCs (blue: ΔChronos $\leq$
1036 -0.05, $P < 0.05$; red: ΔChronos $\geq$ 0.05, $P < 0.05$ from Welch's two-tailed unpaired t-test).

1037 ## Methods

1038 **Cell lines**
1039 H460 (ATCC® HTB-177; RRID:CVCL_0459), PC3 (ATCC® CRL-1435, RRID:CVCL_0035), 786-O (ATCC® CRL-
1040 1932™; RRID:CVCL_1051), 293T (ATCC® CRL-11268™; RRID:CVCL_0063), Caki-1 (ATCC® HTB-46™;
1041 RRID:CVCL_0234), UOK109 (Dr. W. Marston Linehan's laboratory, National Cancer Institute;
1042 RRID:CVCL_B087), UOK146 (Dr. W. Marston Linehan's laboratory, National Cancer Institute,
1043 RRID:CVCL_B123), s-TFE (RIKEN, #RCB4699, RRID:CVCL_R854), ASPS-1 (Dr. Robert H Shoemaker's
1044 laboratory, National Cancer Institute; RRID:CVCL_S738), and ASPS-KY (RIKEN, #RCB5683, RRID:CVCL_S737)
1045 cell lines were cultured at 37°C in DMEM with 10% FBS, 100 U/mL penicillin, and 100 µg/mL Normocin
1046 (#NC9390718). The FU-UR-1 (Dr. Masako Ishiguro's laboratory, Fukuoka University School of Medicine,
1047 RRID:CVCL_6997) cell line was cultured at 37°C in DMEM/F12 (1:1) with 10% FBS, 100 U/mL penicillin, and 100
1048 µg/mL Normocin.

1049 **Genome-scale CRISPR knockout screens**
1050 For the UOK109, FU-UR-1, and s-TFE cell lines, Cas9-expressing cells were constructed as follows: each
1051 parental cell line was seeded in 12-well plates (2.5 × 10^5 cells/well) and incubated at 37°C overnight. The
1052 following day, the medium was replaced, and cells were incubated with lentivirus corresponding to the
1053 pLX_311-Cas9 plasmid (RRID:Addgene_96924), which encodes the Cas9 protein, and 0.8 µg/mL polybrene.
1054 After overnight incubation at 37°C, the cells were trypsinized the following day and cultured in selective media
1055 containing 5 µg/mL blasticidin. After selection, Cas9 expression and activity were confirmed in each
1056 transduced cell line via western blotting and a Cas9-activity assay as described in a previous reference (121).

1057 The Broad Institute Brunello sgRNA library (77,441 sgRNAs targeting 19,114 genes with 1,000 non-targeting
1058 control sgRNAs) was applied for the CRISPR Screen (122,123). UOK109, FU-UR-1, and s-TFE cells were seeded
1059 into 12-well plates at a density of 1.5/1.25/1.5 x 10^6 cells/well, with 1.2 µg/mL polybrene and virus titrated at
1060 MOI <0.3 and spun at 1000 xg for 2 hours at 33°C. After spinfection, 1 mL medium was added to each well and
1061 incubated at 37°C overnight. The following day, all cells were trypsinized and expanded into 15 cm plates at 4
1062 x 10^6 cells/plate with 4/5/5 µg/mL puromycin for a week. Medium with puromycin was replaced every 3 days.
1063 After puromycin selection, cells were seeded at 3 x 10^6 cells/plate and replated every 7 days in 15 cm plates
1064 for 21 days. At 28 days post-infection, cells were collected and stored at -20°C before genomic DNA was
1065 collected.

1066 Genomic DNA was collected with Takara NucleoSpin Blood Kits (Macherey-Nagel), following the
1067 manufacturer's protocol. Before sequencing, genomic DNA samples were amplified by PCR.

1068 **Lentiviral production**
1069 All sgRNAs were cloned into plentiCRISPRv2 (RRID:Addgene_52961, puromycin resistance) as described
1070 (124,125). Sequence of primers for sgRNA cloning are listed in **Supplementary Table S2**. All the constructs
1071 were confirmed by Sanger sequencing.

1072 Lentivirus was prepared by transfecting 293T cells with three plasmids: plentiCRISPRv2
1073 (RRID:Addgene_86153), psPAX2 (RRID:Addgene_12260), and pMD2.G (RRID:Addgene_12259) using
1074 polyethylenimine (PEI). Media was replaced with standard growth media after 12 hours, and supernatant
1075 containing the virus was collected 48 hours post-transfection.

1076 **Validation of genome-scale CRISPR-Cas9 screens and dependency predictions**

1077 PC3, H460, Caki-1, 786-O, UOK109, UOK146, FU-UR-1, s-TFE, and ASPS-1 cell lines were transduced with
1078 lentivirus expressing CRISPR-Cas9 and sgRNA targeting the gene of interest, selected by puromycin, and then
1079 seeded in 96-well plates for confluence and proliferation assays with cell densities of 400-2,000 cells/well
1080 depending on the cell line. On days 7-28, depending on the cell line, cell growth medium was removed from

1081 the plates and the Cell Titer Glo reagent (Promega, #G7571) was added following the user's instructions. Plates
1082 were then shaken at room temperature for 10 minutes. Luminescence was measured on a SpectraMax plate
1083 reader. For cell confluence assays, cell confluence on each plate was determined using a Celigo Imaging
1084 Cytometer daily.

1085 For drug assays, cells were incubated with milademetan (MCE: #HY-101266) or murizatoclax (MCE: #HY-
1086 109184) for 3 days as indicated. Cell Titer Glo assay was measured using a SpectraMax plate reader.

1087 **Competition assay**
1088 Caki-1, 786-O, UOK109, FU-UR-1, and s-TFE were transduced with lentivirus expressing GFP, CRISPR-Cas9,
1089 and sgRNA (either control sgRNA (098) or sgRNA against TFE3). After 3 days, the GFP-positive rate was
1090 measured by a Fortessa flow cytometer to ensure it was higher than 90%. Seven days after viral infection, viral-
1091 infected cells were mixed with non-infected parental cells in a 1:1 ratio. Mixed cells were plated in 6-well
1092 plates. On days 3-24, cells were trypsinized and resuspended in 4% FACS buffer (FBS/PBS), and the GFP-
1093 positive rate was measured by a Fortessa flow cytometer. All flow cytometry data were analyzed with FlowJo
1094 (RRID:SCR_008520). GFP positive percentage in each condition at each time point was first normalized to
1095 value in that condition at d0, and then normalized to sgControl.

1096 **Colony Formation Assays**
1097 PC3, H460, Caki-1, 786-O, UOK109, UOK146, FU-UR-1, s-TFE, and ASPS-1 cell lines were transduced with
1098 lentivirus expressing CRISPR-Cas9 and sgRNA targeting the gene of interest, selected by puromycin, and then
1099 seeded in 12-well plates at various cell densities of 500-6,000 cells/well depending on the cell line. Media was
1100 replaced every 7 days. After 10-28 days, medium was aspirated, and cells were fixed and stained with 0.5%
1101 crystal violet in 25% (volume) methanol solution for about 15 minutes. Stained cells were washed with water
1102 and air-dried. Plates were scanned with an Epson scanner and quantified using ImageJ (RRID:SCR_003070).

1103 **Chronos Score Calculation**
1104 Log_2(fold-changes) in sgRNA abundance on day 28 of the screen were calculated using MAGeCK (126), using
1105 plasmid DNA as a reference. Exome sequencing data was aligned to hg38 using bwa mem (127), and copy-
1106 number was calculated using PureCN (128), as previously described (44). Chronos was used to normalize
1107 log_2(fold-changes) in sgRNAs with segmental copy-number correction (31). ccRCC cell lines were defined
1108 based on Cellosaurus NCIt disease type and included: OSRC2, CAKI2, SLR23, KMRC20, UOK101, SLR24,
1109 KMRC3, CAKI1, TUHR10TKB, SLR26, KMRC1, KMRC2 (RRID:CVCL_2984), SNU349, UMRC3, and RCCFG2.

1110 **Support Vector Regression Model**
1111 Model development and evaluation

1112 The DepMap (RRID:SCR_017655) 23Q2 expression matrix (converted to log_2(TPM+1), https://depmap.org) and
1113 23Q2 CRISPR-KO dependency score matrix (Chronos-normalized, https://depmap.org) were downloaded and
1114 subset to shared cell lines. We split these data into 5 equal subsets for 5-fold cross-validation (four training
1115 folds and evaluation on a validation fold). Expression was Z-scored for each gene. For each gene, a new model
1116 was trained to predict its dependency score.

1117 To reduce dimensionality, we first calculated the Pearson correlation coefficient between each feature (i.e. Z-
1118 scored gene expression) and the dependency score of the gene being analyzed in the training data. The top
1119 predictive features for each gene (ranked by absolute value of Pearson correlation coefficient, 5000 in final
1120 model [a number that we varied to maximize performance], see **Supplementary Fig. S3B**) were determined.

1121 For each gene, we subset the training data to these top features and trained a support vector regression model
1122 (sklearn.svm.SVR, RBF kernel) to predict dependency scores. We tested a variety of other models from sklearn
1123 including SVR with a linear kernel, ridge regression, lasso regression, elastic net, and k-nearest neighbors
1124 regression (**Supplementary Fig. S3B**). Performance on the validation fold was assessed by Pearson

correlation between predicted and observed (i.e. experimentally determined) Chronos scores for each gene across all cell lines in the validation fold. We repeated this process four more times (changing the validation fold) during cross-validation. Performance metrics were averaged between these five models for each gene. SVR with an RBF kernel had the best performance across all models tested with 657 genes being highly predictable (defined as R ≥ 0.4 between predicted and observed Chronos scores) (**Supplementary Fig. S3b**). The average Pearson correlation coefficient for predicted vs. observed Chronos score was R=0.16 across 16845 genes. The correlation between predicted and observed Chronos score across all gene-cancer cell line pairs in the test data was R = 0.92. Specifics and code for the developed pipeline as well as scripts for interactive visualization of predicted dependencies in this manuscript are available in Github: https://github.com/SViswanathanLab/TrPLet.

Model deployment

The models for each gene were retrained on the entire DepMap dataset prior to testing on external datasets. To calculate approximate coefficients from the model, we used a kernel trick taking the linear combination of support vector weighted by dual coefficients from RBF kernel. Broadly, our model was applied to three types of data: (1) TCGA tumor RNA-seq, (2) non-TCGA tumor RNA-seq, (3) cell line RNA-seq. (1) For TCGA tumor RNA-seq, we Z-scored the expression of each gene ($\log_2$(TPM+1)) within TCGA and predicted on the resulting normalized expression data. Clustering (two-component t-SNE) based on dependency scores (predicted: TCGA, experimentally-derived via CRISPR screen: DepMap) using this approach resulted in TCGA tumors clustering with screened cell lines from DepMap of the same lineage (see **Supplementary Fig. S6A**). (2) For non-TCGA tumor RNA-seq, we downloaded RNA-seq fastq files or count matrices when present, from the Gene Expression Omnibus (GEO; RRID:SCR_005012). Reads were aligned to GENCODE (RRID:SCR_014966) v38 transcript reference using STAR/RSEM (129,130). The resulting count matrices were inner joined with the TCGA count matrix (131) (https://osf.io/gqrz9/files/osfstorage), and batch corrected using ComBat-seq (132) using lineage as a covariate (for this purpose, tRCCs, Wilms' tumors, CDC, and RMC were classified as "KIRP"; ASPS, PEComa, and EHE were classified as "SARC"; ccRCC was classified as "KIRC"). The counts were then normalized to gene-level transcripts per kilobase million (TPM), converted to $\log_2$(TPM+1), and each gene's expression was then Z-scored (across the combined matrix consisting of the external dataset and TCGA). The resulting Z-scored expression in the external dataset was then used for prediction, as described above. (3) For cell line RNA-seq, a gene-level normalized expression matrix ($\log_2$(TPM+1)) was either downloaded or generated from STAR/RSEM. The expression of each gene in the resulting matrix was scaled (Z-scored) using the mean/standard deviation calculated when scaling the DepMap expression matrix. The resulting Z-scored expression values were used for prediction. Batch correction was forgone in this use-case based on tSNE clustering of tRCC cell lines with kidney cell lines in DepMap, and ASPS cell lines with soft tissue and CNS cell lines in DepMap based on expression profile (**Supplementary Fig. S6K**).

Survival Analysis

Count matrices from CM-025 (133) were used to predict MTOR dependency in ccRCC samples. Outcomes (overall survival, progression-free survival) between groups were compared using lifelines (134). Blinding, randomization not relevant to this study because analysis of these data was retrospective. Analyses were not stratified by sex as a biological variable.

Supplementary Figures and Captions

Supplementary Fig. S1 | Defining dependencies in tRCC and ccRCC

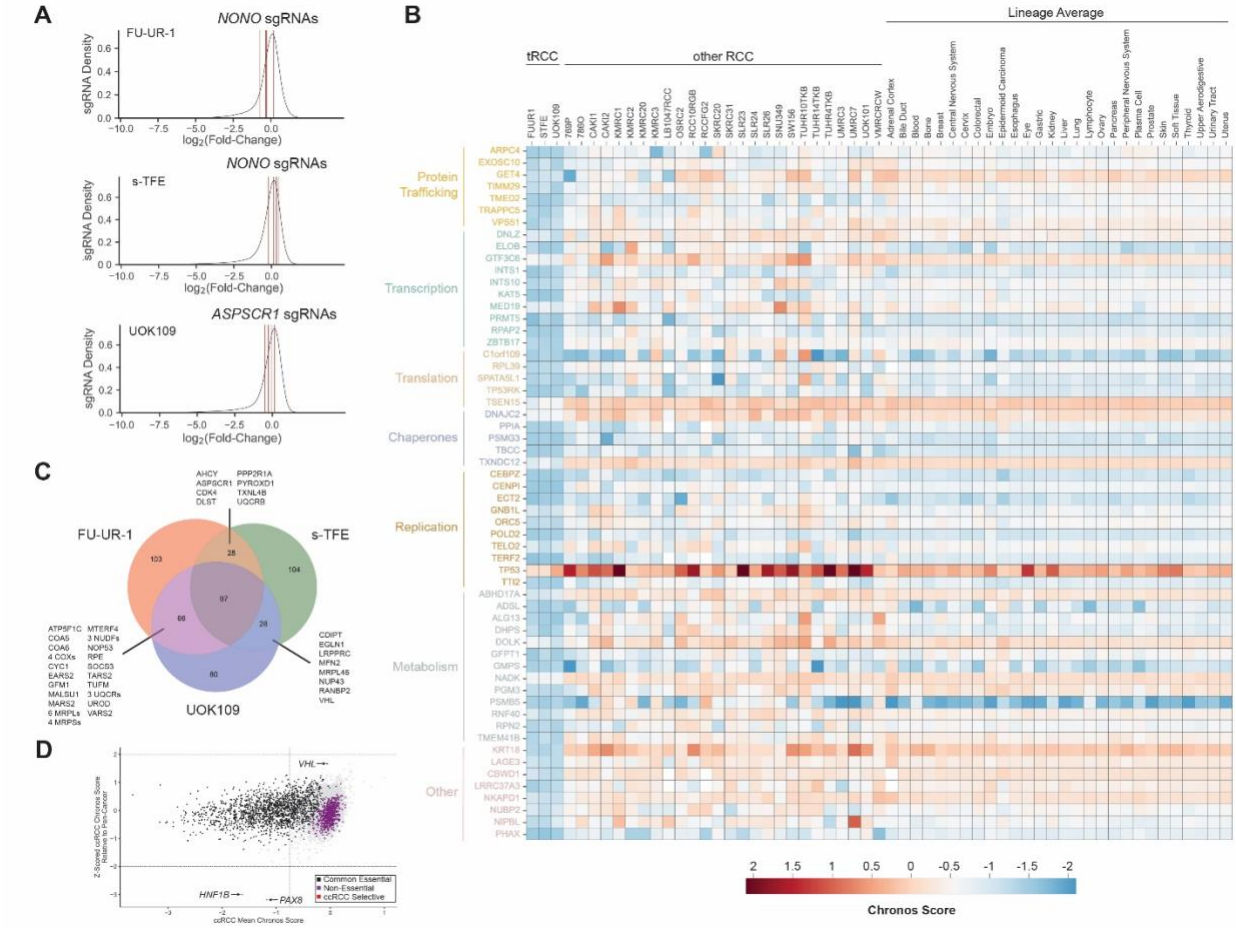

(A) Log-fold change for individual sgRNAs targeting *NONO* in tRCC cell lines harboring an *ASPSCR1-TFE3* fusion (FU-UR-1; s-TFE) and log-fold change for sgRNAs targeting *ASPSCR1* in a cell line harboring a *NONO*-TFE3 fusion (UOK109). Density plot shows the distribution for LFC of all sgRNAs assessed in the CRISPR screen in each cell line while vertical lines represent log-fold change for individual sgRNAs. All sgRNAs are contained within the oncogenic fusion in cell lines with the fusion.

(B) Heat map of tRCC-selective dependencies (defined as genes with ΔChronos ≤ -0.5 between every tRCC cell line and DepMap ccRCC mean), for selected pathways (remaining genes/pathways shown in **Fig.2E**). Chronos scores for individual tRCC cell lines, DepMap RCC cell lines, and average Chronos score for individual lineages screened in DepMap are shown for reference.

(C) Venn diagram of selective dependencies in tRCC cell lines screened (defined as genes with ΔChronos ≤ -0.5 between an individual tRCC cell line and DepMap ccRCC mean).

(D) Mean Chronos score for each gene across the DepMap ccRCC cell lines is plotted against the Z-scored Chronos score for that gene (Z-score calculated relative to all DepMap cell lines). Non-essential genes are

1185 colored purple while common essential genes are colored black. *HNF1B and PAX8* represent the two
1186 strongest dependencies in ccRCC relative to cancer cell lines of other lineages.

Supplementary Fig. S2 | Additional validation of tRCC selective dependencies

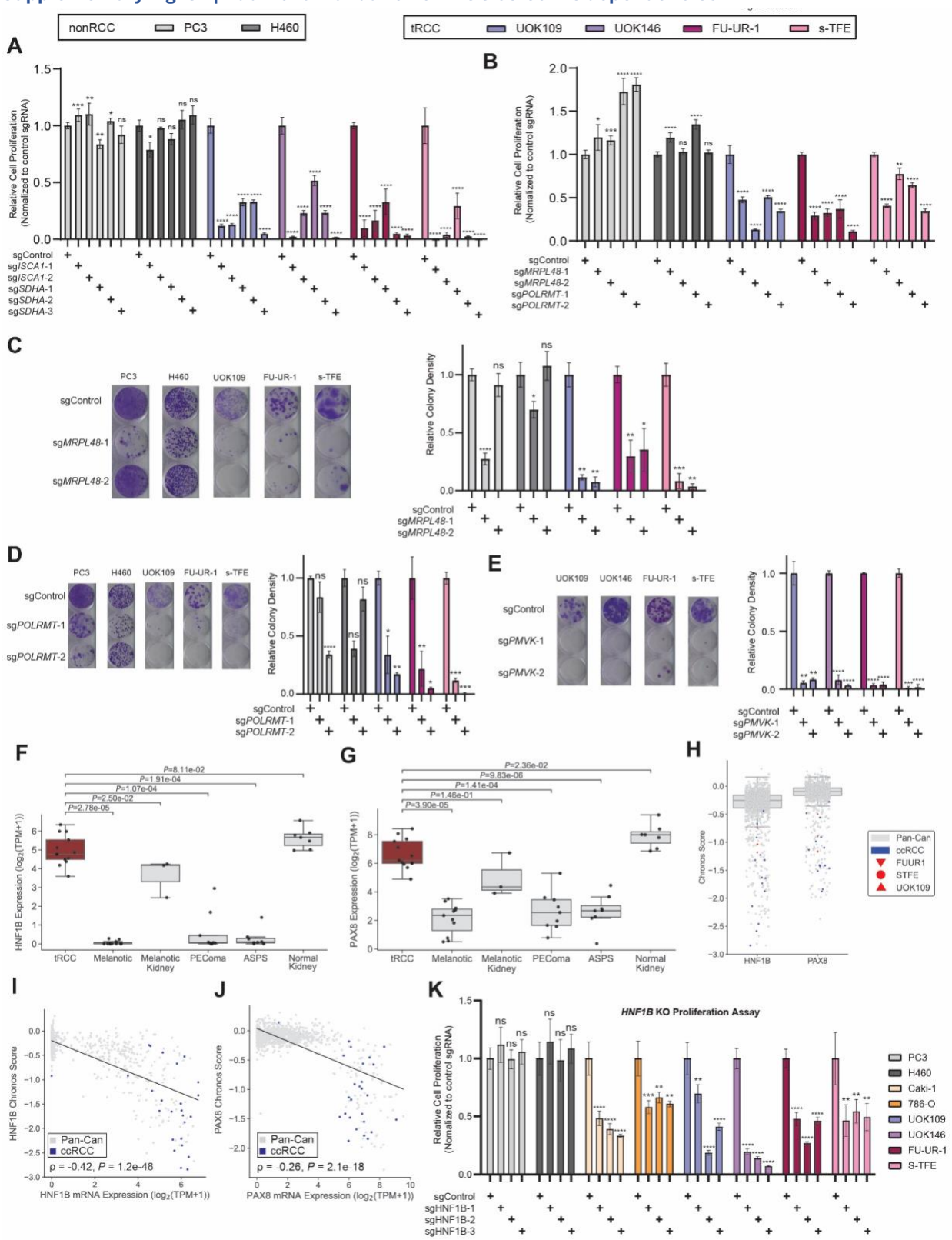

(A-B) Relative viability of non-RCC cells (PC3, H4b60) or tRCC cells (UOK109, UOK146, FU-UR-1, s-TFE) after CRISPR/Cas9 knockout of *ISCA1* **(A)**, *SDHA* **(A)**, *MRPL48* **(B)** or *POLRMT* **(B).** Viability is normalized to control sgRNA, shown as mean +/- s.d., n=6 biological replicates per condition. *P*-values were calculated by Welch's (two-tailed unpaired) t-test as compared with sgControl samples. **P* < 0.05, ***P* < 0.01, ****P* < 0.001, *****P* < 0.0001.

(C-D) Representative photograph (left) and quantification of colony formation assay (right) for of non-RCC cells (PC3, H460) or tRCC cells (UOK109, FU-UR-1, s-TFE) after CRISPR/Cas9 knockout of *MRPL48* **(c)** or *POLRMT* **(D)**. Shown as mean +/- s.d., n=3 biological replicates per condition. *P*-values were calculated by Welch's (two-tailed unpaired) t-test as compared with sgControl samples. **P* < 0.05, ***P* < 0.01, ****P* < 0.001, *****P* < 0.0001.

(E) Representative photograph (left) and quantification of colony formation assay (right) for tRCC cells (UOK109, UOK146, FU-UR-1, s-TFE) after CRISPR/Cas9 knockout of *PMVK*. Shown as mean +/- s.d., n=3 biological replicates per condition. *P*-values were calculated by Welch's (two-tailed unpaired) t-test as compared with sgControl samples. **P* < 0.05, ***P* < 0.01, ****P* < 0.001, *****P* < 0.0001.

(F-G) In a published RNA-seq dataset (67), the expression of *HNF1B* **(A)** and *PAX8* **(B)** are shown ($\log_2$(TPM+1)) across kidney-derived *TFE3* fusion tumors (tRCC, melanotic kidney), normal kidney tissue, and other TFE3-driven tumors (PEComa, ASPS, Melanotic).

(H) Distribution of Chronos scores for *HNF1B* and *PAX8* across DepMap cell lines and tRCC cell lines. ccRCC cell lines are shown in blue, tRCC cell lines are shown in red.

(I-J) Correlation between *HNF1B* **(I)** or *PAX8* **(J)** Chronos score and gene expression ($\log_2$(TPM+1)) across DepMap cell lines. ccRCC cell lines are shown in blue. *P*-values computed by Spearman's rho test.

(K) Viability of nonRCC cells (PC3, H460), ccRCC cells (Caki-1 and 786-O) or tRCC cells (UOK109, UOK146, FU-UR-1, s-TFE) after *HNF1B* knockout. Viability was measured by CellTiter-Glo; n=6 replicates per condition. *P*-values were calculated by Welch's (two-tailed unpaired) t-test as compared with sgControl samples. **P* < 0.05, ***P* < 0.01, ****P* < 0.001, *****P* < 0.0001.

Supplementary Fig. S3 | Performance Metrics for dependency prediction and application to RNA-seq datasets

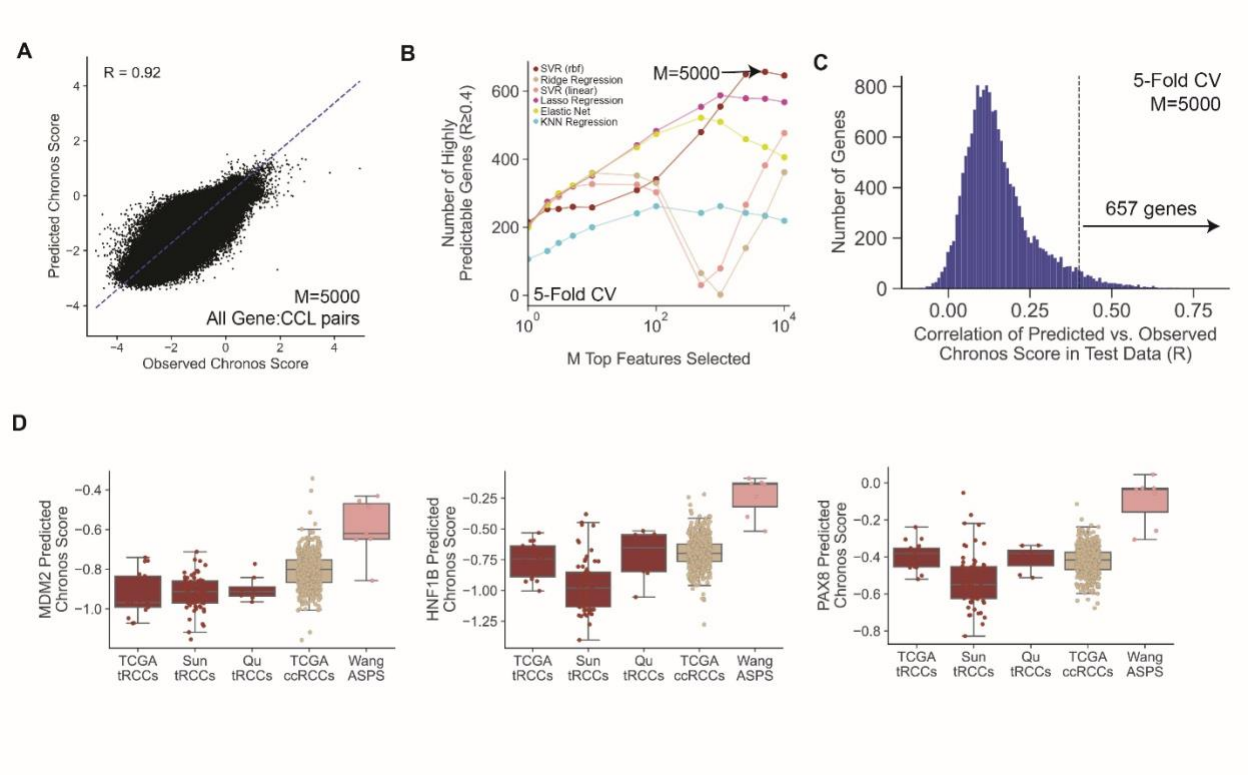

(A) Correlation between observed Chronos score on experimental CRISPR screening and Chronos score predicted by our model across 1121 cell lines. Each point represents a Chronos score for one gene dependency in one cell line.

(B) Number of predicable genes by with R ≥ 0.4 between predicted and experimentally-derived Chronos score (averaged from 5-fold cross-validation) based on number of features used for prediction (M) and machine learning model tested. SVR with an RBF kernel using the 5000 top features were selected for this study, as this maximizes the number of highly predicable gene dependencies (N=657).

(C) Distribution of correlation coefficient between observed and predicted Chronos score for each gene across all cell lines in DepMap (averaged from 5-fold cross-validation, 5000 top features for each gene predicted). 657 genes are highly predicable with an R ≥ 0.4 (threshold used for this study).

(D) Predicted Chronos scores from tumor samples in either tRCC (TCGA, Sun et al., Qu et al.), ccRCC (TCGA), or ASPS (Wang et al.) RNA-Seq cohorts (27,28,59,67) for the following genes: *MDM2*, *HNF1B*, *PAX8*.

Supplementary Fig. S4 | Validation of *MDM2* and *KMT2D* dependencies in a subset of tRCCs.

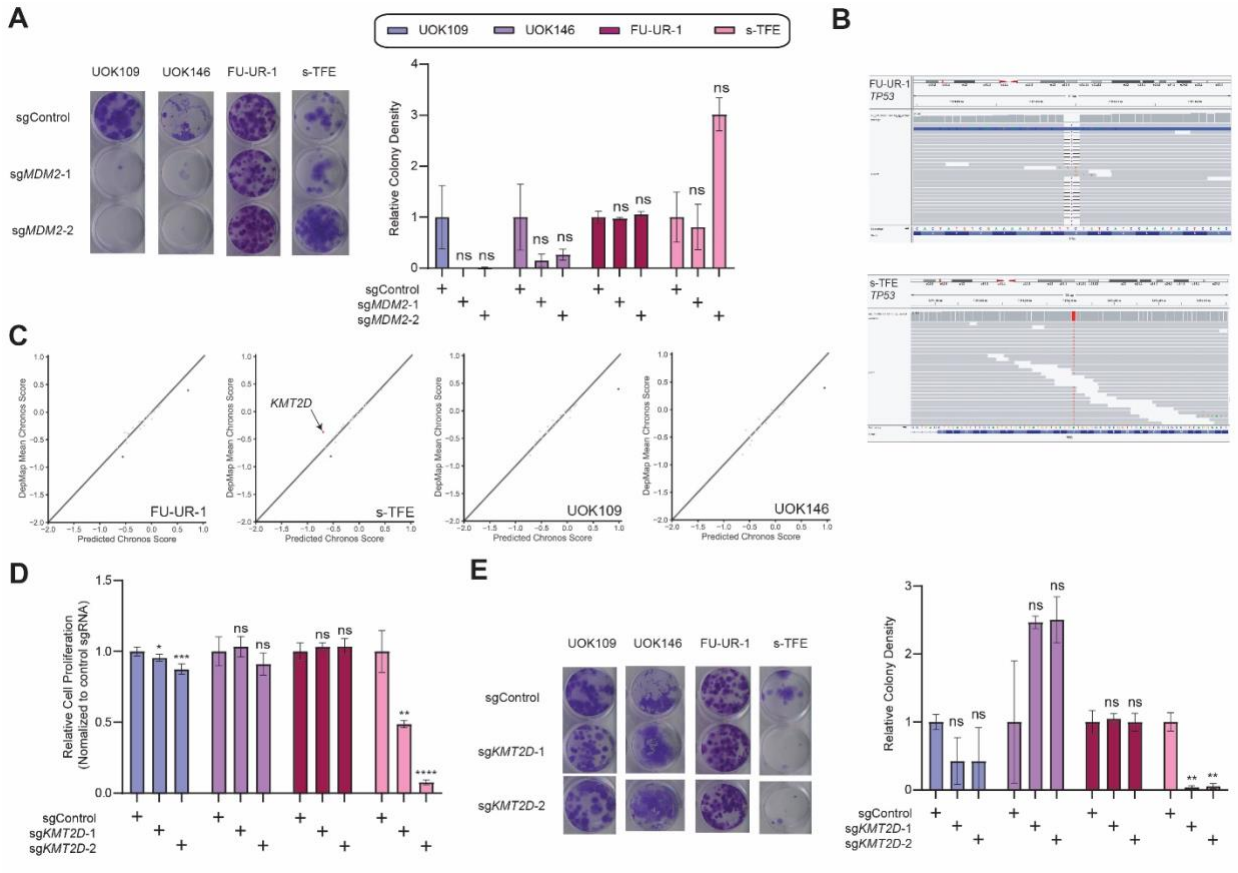

(A) Representative photograph (left) and quantification of colony formation assay (right) for tRCC cells (UOK109, UOK146, FU-UR-1, s-TFE) after CRISPR/Cas9 knockout of *MDM2*. Shown as mean +/- s.d., n=3 biological replicates per condition. *P*-values were calculated by Welch's (two-tailed unpaired) t-test as compared with sgControl samples. **P* < 0.05, ***P* < 0.01, ****P* < 0.001, *****P* < 0.0001.

(B) IGV snapshots showing mutations at the *TP53* locus in FU-UR-1 and s-TFE cells.

(C) Chronos score for 20 genes previously reported to be somatically altered in tRCC (23,44) were predicted by our model (red: ΔChronos ≤ -0.2; blue: ΔChronos ≥ 0.2 between predicted and DepMap mean). Predicted Chronos scores in each tRCC cell line are plotted against mean Chronos scores across all DepMap cell lines (as assessed by genome-scale CRISPR screening).

(D) Relative viability of tRCC cells (UOK109, UOK146, FU-UR-1, s-TFE) after CRISPR/Cas9 knockout of *KMT2D*. Viability is normalized to control sgRNA, shown as mean +/- s.d., n=6 biological replicates per condition. *P*-values were calculated by Welch's (two-tailed unpaired) t-test as compared with sgControl samples. **P* < 0.05, ***P* < 0.01, ****P* < 0.001, *****P* < 0.0001.

(E) Representative photograph (left) and quantification of colony formation assay (right) for tRCC cells (UOK109, UOK146, FU-UR-1, s-TFE) after CRISPR/Cas9 knockout of *KMT2D*. Shown as mean +/- s.d., n=3 biological replicates per condition. *P*-values were calculated by Welch's (two-tailed unpaired) t-test as compared with sgControl samples. **P* < 0.05, ***P* < 0.01, ****P* < 0.001, *****P* < 0.0001.

Supplementary Fig. S5 | Selective dependencies in other cancer types

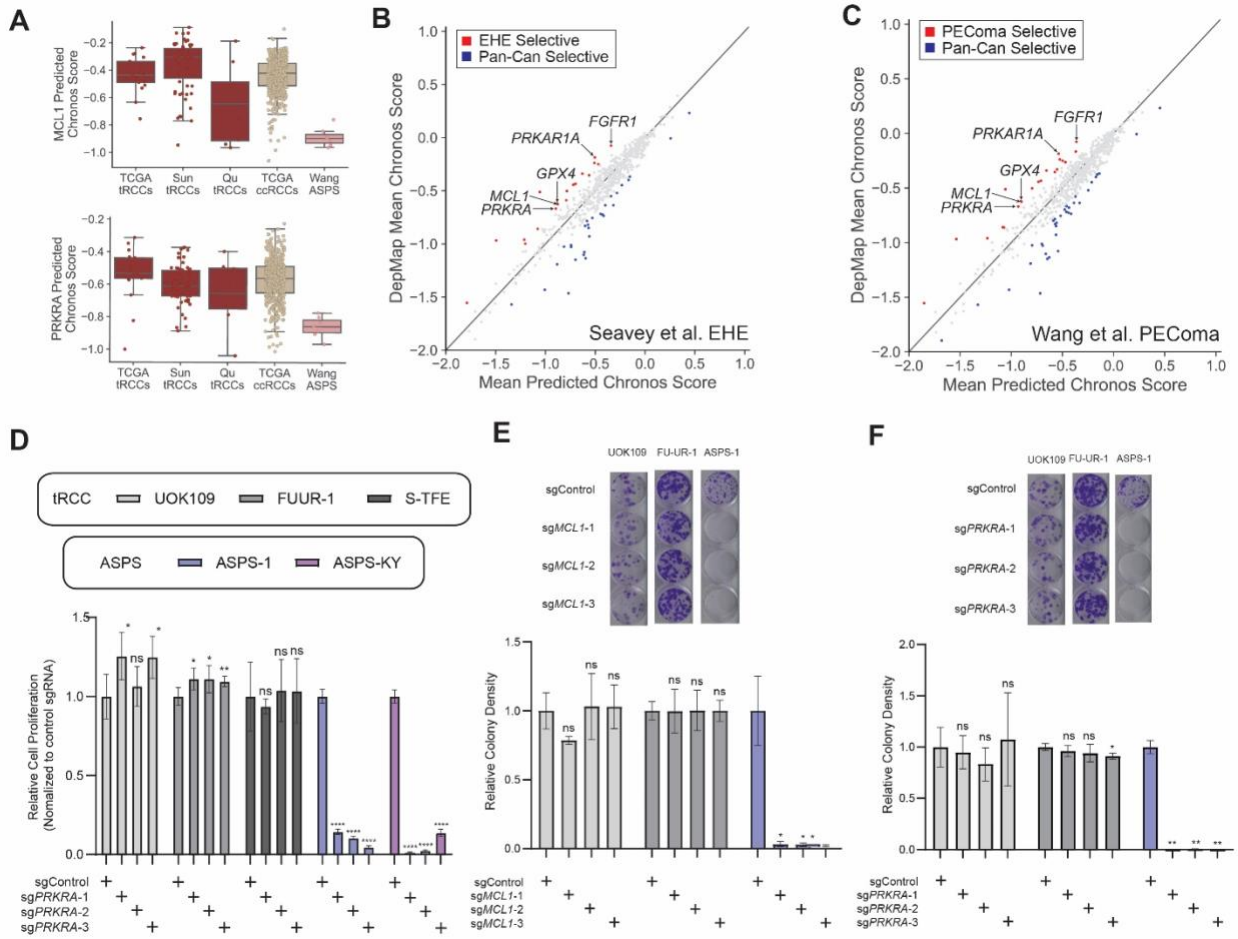

(A) Predicted Chronos scores from tumor samples in either tRCC (TCGA, Sun et al., Qu et al.), ccRCC (TCGA), or ASPS (Wang et al.) RNA-Seq cohorts (27,28,59,67) for the following genes: *MCL1, PRKRA*.

(B-C) Mean predicted Chronos scores in EHE tumors (135) **(B)** or PEComa tumors (67) **(C)** are plotted against mean Chronos score across all DepMap cell lines (as assessed by genome-scale CRISPR screening). Chronos scores for 657 genes were predicted by our model (red: ΔChronos ≤ -0.2; blue: ΔChronos ≥ 0.2 between mean predicted Chronos score and DepMap mean).

(D) Proliferation of tRCC cells (UOK109, FU-UR-1, s-TFE) and ASPS cell lines (ASPS-1 and ASPS-KY) transduced with one of 3 distinct sgRNAs targeting *PRKRA* or a non-targeting sgRNA control. n = 6 biological replicates per condition. *P*-values were calculated by Welch's (two-tailed unpaired) t-test as compared with sgControl samples. **P* < 0.05, ***P* < 0.01, ****P* < 0.001, *****P* < 0.0001.

(E-F) Representative photograph (top) and quantification of colony formation assay (bottom) for of tRCC cells (UOK109, FU-UR-1) or ASPS cells (ASPS-1) after CRISPR/Cas9 knockout of *MCL1* **(E)** and *PRKRA* **(F)**. Shown as mean +/- s.d., n=3 biological replicates per condition. *P*-value were calculated by Welch's (two-tailed unpaired) t-test as compared with sgControl samples. **P* < 0.05, ***P* < 0.01, ****P* < 0.001, *****P* < 0.0001.

Supplementary Fig. S6 | Application of dependency prediction across cell lines, tumors, and to predict therapy response

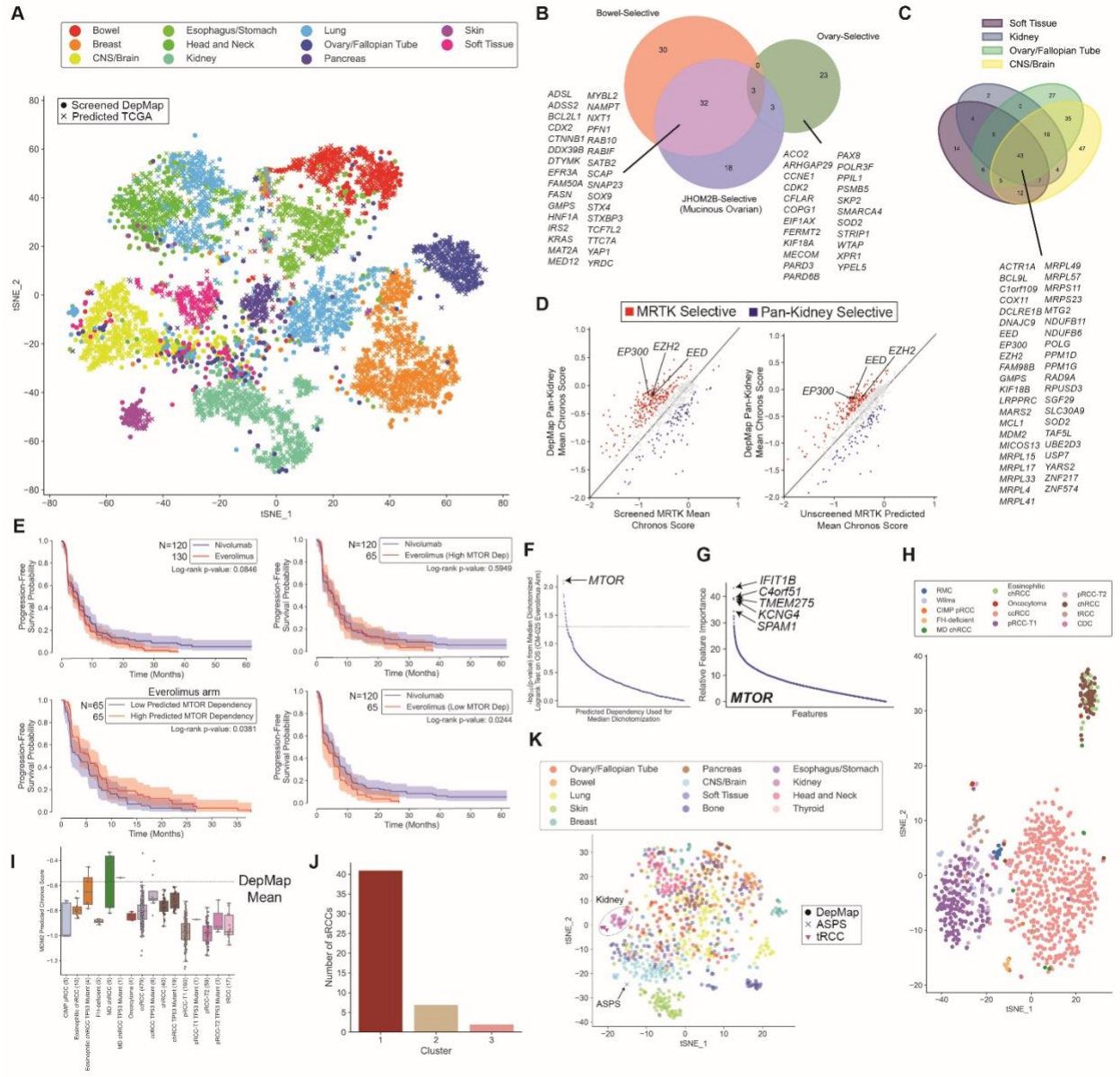

(A) *t*-SNE projection based on dependency score for 657 PD genes for cell lines experimentally screened in the DepMap (N=778, circle) or cell lines for which dependencies were predicted in TCGA (N=6498, cross). Cell lines are colored based on annotated lineage, with 11 common lineages (shared between TCGA and DepMap; hematological lineages not included) shown.

(B) Predicted dependencies in a cell line of reported mucinous ovarian origin (JHOM2B; not screened in the DepMap) overlap more strongly with bowel-selective dependencies than ovary-selective dependencies (as assessed by genome-scale CRISPR screening). Genes are included in the Venn diagram if ΔChronos ≤ -0.2 between group (JHOM2B or lineage) mean and DepMap mean.

1282 **(C)** Predicted dependencies in MRTK cell lines (not screened in the DepMap, "Kidney") overlap strongly with
1283 dependencies in cell lines of distinct lineages (as assessed by genome-scale CRISPR screening) in the same
1284 cluster in dependency space (from **Fig. 5C**). Genes are included in the Venn diagram if ΔChronos ≤ -0.2
1285 between group mean and DepMap mean.

1286 **(D)** *Left*: Mean Chronos scores in screened MRTK cell lines in DepMap are plotted against mean Chronos
1287 scores across pan-kidney cell lines in DepMap (as assessed by genome-scale CRISPR screening, MRTK
1288 excluded). *Right*: Mean predicted Chronos scores in unscreened MRTK cell lines in DepMap are plotted against
1289 mean Chronos scores across pan-kidney cell lines in DepMap (as assessed by genome-scale CRISPR
1290 screening, MRTK excluded). Restricted to 657 highly predictable genes in both plots (red: ΔChronos ≤ -0.2;
1291 blue: ΔChronos ≥ 0.2 between mean (predicted) Chronos score and DepMap mean).

1292 **(E)** Progression-free survival (PFS) for patients in CM-025, comparing nivolumab or everolimus treatment
1293 arms stratified by predicted *MTOR* dependency score as indicated. Predicted *MTOR* dependency score was
1294 median dichotomized to obtain high and low predicted dependencies (133,136,137). *P*-values calculated by
1295 log-rank test.

1296 **(F)** Waterfall plot of -$\log_{10}$(*P*-value) from log-rank test comparing overall survival of patients in CM-025, with
1297 everolimus arm stratified by predicted dependency score for each of the 657 PD genes and *MTOR*. Predicted
1298 dependency scores were median dichotomized (133,136,137).

1299 **(G)** Relative feature importance (ranked across 5000 top features) for all RNA-seq based predictors of *MTOR*
1300 Chronos score (see **Methods**). Each point represents an individual feature.

1301 **(H)** *t*-SNE projection based on RNA-seq expression for kidney tumors with predicted dependencies (N=851,
1302 cross). Tumors are colored based on annotated subtype, and clusters are indicated.

1303 **(I)** Box plot of predicted *MDM2* Chronos score across TCGA kidney cancers stratified by annotated *TP53*
1304 mutation status. DepMap mean Chronos score for *MDM2* is indicated as a dotted line.

1305 **(J)** Number of S/R RCCs that fall within each dependency cluster shown in **Fig. 6B** (94).

1306 **(K)** *t*-SNE projection based on RNA-seq expression for tRCC cell lines (N=4) and ASPS cell lines (N=2) analyzed
1307 in this study with 769 cell lines across 13 common solid tumor lineages in DepMap.

1308

Supplementary Table Captions

Supplementary Table S1 Chronos scores for tRCC cell lines screened in this study (Tab 1), tRCC-selective dependencies (Δ(Chronos) ≤ -0.5 for every individual cell line) relative to DepMap ccRCC (Tab 2), and relative to DepMap pan-cancer (Tab 3).

Supplementary Table S2 sgRNA sequences used in this study.

Supplementary Table S3 Gene-level performance (correlation between predicted and observed Chronos score) for all genes.

Supplementary Table S4 Predicted Chronos scores for 657 PD genes for individual cell lines/tumors in all analyzed cohorts (tab 1: tRCC cell lines, tab 2: TCGA tRCC tumors (23), tab 3: Sun et al. tRCC tumors (27), tab 4: Qu et al. tRCC tumors (28), tab 5: ASPS cell lines, tab 6: Wang et al. ASPS tumors (67), tab 7: Wang et al. PEComa tumors (67), tab 8: Seavey et al. EHE tumors (135), tab 9: TCGA (138), tab 10: TCGA CIMP-pRCC (59), tab 11: TCGA FH-deficient RCC (139), tab 12: TCGA MD-chRCC (59), tab 13: TCGA eosinophilic chRCC (140), tab 14: TCGA oncocytoma (141), tab 15: TCGA ccRCC (59), tab 16: TCGA pRCC-T1 (59), tab 17: TCGA pRCC-T2 (59), tab 18: TCGA chRCC (59), tab 19: Wang et al. CDC (120), tab 20: Coutinho et al. Wilms' tumors (119), tab 21: Msaouel et al. RMC (118), tab 22: TCGA S/R RCC (94), tab 23: unscreened CCLE (82)).

Note: Due to its large size, **Table S4** can be downloaded at the following link:
https://datadryad.org/stash/share/AXSCxqhZBRDNu-046B0YBKKlPa8aHJfT7zwWCy6FSPs